Title: Dynamic Rupture Modeling in a Complex Fault Zone with Distributed and Localized Damage

Author: Chunhui Zhao

Department of Civil and Environmental Engineering
University of Illinois, Urbana-Champaign

Author: Md Shumon Mia

Department of Civil and Environmental Engineering
University of Illinois, Urbana-Champaign

Author: Ahmed Elbanna

Department of Civil and Environmental Engineering
University of Illinois, Urbana-Champaign

Author: Yehuda Ben-Zion

Department of Earth Sciences and Statewide California Earthquake Center
University of Southern California

Corresponding Authors: Ahmed Elbanna and Yehuda Ben-Zion

The paper is a non-peer reviewed preprint submitted to EarthArXiv, and peer reviewed preprint submitted to Mechanics of Materials journal.

Highlights

- We combine a continuum damage-breakage rheology model in our in-house dynamic rupture simulator adopting linear slip weakening friction law for the current study.
- We quantify the effects of damage and breakage using spatial-temporal distribution of particle velocity and wave-speed reduction.
- The results highlight the growth of localization bands and the competing effects between localized fault slip and inelastic bulk deformation.
- Comparisons between continuum damage-breakage model and plasticity reveal that higher slip, slip rate, increased energy radiation and decreased energy dissipation can be observed in damage-induced softening stage.

Dynamic Rupture Modeling in a Complex Fault Zone with Distributed and Localized Damage

Chunhui Zhao[a], Mid Shumon Mia[a], Ahmed Elbanna [1a], Yehuda Ben-Zion [1b]

[a]*Department of Civil and Environmental Engineering, University of Illinois, Urbana-Champaign, 61801, Illinois, USA*
[b]*Department of Earth Sciences, University of Southern California, Los Angeles, 90007, California, USA*

Abstract

Active fault zones have complex structural and geometric features that are expected to affect earthquake nucleation, rupture propagation with shear and volumetric deformation, and arrest. Earthquakes, in turn, dynamically activate co-seismic off-fault damage that may be both distributed and localized, affecting fault zone geometry and rheology, and further influencing post-seismic deformation and subsequent earthquake sequences. Understanding this co-evolution of fault zones and earthquakes is a fundamental challenge in computational rupture dynamics with consequential implications for earthquake physics, seismic hazard and risk. Here, we implement a continuum damage-breakage (CDB) rheology model in our MOOSE-FARMS dynamic rupture simulator to investigate the interplay between bulk damage and fault motion on the evolution of dynamic rupture, energy partitioning, and ground motion characteristics. We demonstrate several effects of damage (accounting for distributed cracking) and breakage (accounting for granulation) on rupture dynamics in the context of two prototype problems addressed currently in the 2D plane-strain setting: (1) a single planar fault and (2) a fracture network. We quantify the spatio-temporal reduction in wave speeds associated with dynamic ruptures in each of these cases and track the evolution of the original fault zone geometry. The results highlight the growth and coalescence of localization bands as well as competition between localized slip on the pre-existing faults vs. inelastic deformation in the bulk. We analyze the differences between off-fault dissipation through damage-breakage vs. plasticity and show that damage-induced softening increases the slip and slip rate, suggesting enhanced energy radiation and reduced energy dissipation. These results have important implications for long-standing problems in earthquake and fault physics as well as near-fault seismic hazard, and they motivate continuing towards 3D simulations and detailed near-fault observations to uncover the processes occurring in earthquake rupture zones.

Keywords: Dynamic rupture, brittle damage, complex fault geometry, granular flow, phase transition, friction, fracture

---

[1]Corresponding Authors

1. Introduction

The dynamic inter-play between earthquakes and fault zone structures has long been acknowledged as a critical mechanism in controlling source physics (Ben-Zion, 2008), yet it remains an understudied topic due to the myriad of theoretical and computational challenges involved in such investigation. Active natural faults exist within broader damage zones characterized by a multitude of complex structural and geometric features, which are expected to affect earthquake nucleation, rupture propagation, potential for dilatation and compaction, energy partitioning between dissipation and radiation, and rupture arrest. Earthquakes, in turn, activate co-seismically off-fault damage that may be both distributed and localized, producing changes in fault zone geometry, elasticity and rheology, which influence further energy radiation, post-seismic deformation, and subsequent earthquake sequences.

Several approaches have been proposed to couple the on-fault rupture propagation with off-fault yielding. Examples include: (1) continuum visco-elastic damage frameworks (Lyakhovsky et al., 1997; Hamiel et al., 2004; Hetland and Hager, 2005; Wang et al., 2012; Sun and Wang, 2015). (2) coupled interfacial friction laws and off-fault plasticity (Andrews, 2005; Ben-Zion and Shi, 2005; Duan and Day, 2008; Templeton and Rice, 2008; Ma and Andrews, 2010; Dunham et al., 2011; Kaneko and Fialko, 2011; Xu and Ben-Zion, 2013; Gabriel et al., 2013). (3) models with embedded microcracks that can interact and grow (Bhat et al., 2012; Thomas and Bhat, 2018; Okubo et al., 2019). (4) continuum damage-breakage model developed and used by (Lyakhovsky and Ben-Zion, 2014a,b; Lyakhovsky et al., 2016; Kurzon et al., 2019, 2021), and more recently (5) phase-field models that account for pressure-sensitive frictional response (Fei et al., 2023; Hayek et al., 2023).

The continuum visco-elastic damage models belong to the general class of the Maxwell-Kelvin rheology and its variations with an original focus on ductile deformation. It has been recently adapted to describe quasi-brittle response (Dansereau et al., 2023) by invoking time-dependent variation in the elastic properties through degradation and healing. Plasticity models have proven useful for understanding coseismic inelastic dissipation and how rupture characteristics are influenced by permanent deformation in the bulk. Off-fault plasticity was shown to affect the energy partitioning, the rupture mode (i.e. crack vs. pulses) and rupture characteristics such as the speed of rupture propagation and peak slip rate (Ben-Zion and Shi, 2005; Shi et al., 2010). Recent studies incorporating off-fault plasticity in modeling of sequences of earthquakes and aseismic slip also show that off-fault plasticity evolves with progressive events and influences the seismic cycle in different ways including creating slip deficits (Erickson et al., 2017), changing the nucleation site (Abdelmeguid and Elbanna, 2022a), and generating spatial rupture segmentation and temporal clustering (Mia et al., 2022, 2023).

One limitation of plasticity models for earthquake ruptures is that the bulk material experiences no change in its elastic properties. This is inconsistent with abundant field observations of zones with modified elastic properties around large faults (Ben-Zion and Sammis, 2003; Allam et al., 2014; Zigone et al., 2015; Qiu et al., 2021), along with lab experiments (Gupta, 1973; Lockner and Byerlee, 1980; Stanchits et al., 2006; Aben et al., 2019; Xu et al., 2019) and field studies (Peng and Ben-Zion, 2006; Froment et al., 2013; Pei et al., 2019) that document changes in the elastic wave speeds in the wake of large ruptures. This damage-induced variation in the elastic properties produces an asymmetry between the loading and unloading branches of the stress-strain curve while plasticity does not have this effect (Hamiel et al., 2004; Xu et al., 2015). Moreover, the reduction of elastic moduli in the material surrounding the fault can lead to motion amplification in the damage zone (Ben-Zion and Aki, 1990; Spudich and Olsen, 2001), coupling between slip and dynamic change of normal stress on the fault (Weertman, 1980; Andrews and Ben-Zion, 1997; Shlomai and Fineberg, 2016), and interactions of wave reflections from edges of the damage zone with dynamic ruptures (Ben-Zion and Huang, 2002; Huang and Ampuero, 2011). These effects can significantly impact properties of individual ruptures and earthquake sequences (Ampuero and Ben-Zion, 2008; Bhat et al., 2010; Thakur and Huang, 2021; Aichele et al., 2023; Abdelmeguid and Elbanna, 2022b).

The continuum damage-breakage (CDB) model of (Lyakhovsky and Ben-Zion, 2014a,b; Lyakhovsky et al., 2016) and later works consider visco-elastic damage including variation in the elastic properties, while further incorporating a phase transition of a damaged solid to a granular flow once the damage reaches a critical value. Following earlier studies (Lyakhovsky et al., 1997, 2005), the CDB model also includes a laboratory-based $log(t)$ healing to capture the recovery of elastic moduli as the material unloads during periods of interseismic slow deformation. This enables capabilities for earthquake cycle simulations with more realistic constitutive response. In this paper, we adopt a CDB model formulation with both co-seismic (fast slip) degradation and post-seismic (slow deformation) healing, with a focus on a single dynamic rupture event.

An initial study of the coupling between bulk damage and frictional slip has been performed by (Xu et al., 2015). However, that model was restricted to a single planar fault and considered only visoelastic damage accumulation with no transition to granular-like flow at higher damage levels. A transition to a granular phase within the slip zone is consistent with observations (Ben-Zion and Sammis, 2003) and is important for deformation localization during brittle instabilities and energy dissipation. Here, we consider the effects of breakage and transition to a granular phase on the rupture characteristics and evolution of fault zone structure. We move beyond the single planar fault case and consider also fracture networks. This enables us to investigate the interplay between rupture characteristics with both pre-existing damage and generation of new damage. The modeling is inspired by the pioneering work of (Xu and Needleman, 1994) which enabled, for the first time, the simulation of an arbitrary growth of dynamic fracture by inserting cohesive elements along all mesh interfaces, either apriori or adaptively.

The rest of the paper is organized as follows: In the problem description section, we first explain the strong form of the boundary value problem, with the relevant parameters listed in Table 1. Then we outline the main features of the continuum damage-breakage model combining recent results of (Lyakhovsky et al., 2011; Lyakhovsky and Ben-Zion, 2014a,b; Lyakhovsky et al., 2016). This is followed by brief explanations of the initial and boundary conditions including linear slip weakening friction law on the fault interface, the bulk initial stress field, and the initiation of rupture using an artificial nucleation approach. We then summarize the main model parameters in Table 2. In the results section, we present the geometry setup and simulations for two cases: (1) For a planar fault case, we analyze and compare off-fault damage-breakage results with off-fault Drucker-Prager plasticity, with a focus on rupture characteristics, energy dissipation, and distribution of inelastic strain. (2) For a fault network case, we conduct investigations into favorable rupture activation governed by the strength parameter S, damage localization characteristics, and effects on the fault network through wave radiation and material degradation. Finally, we summarize our findings and their implications in the discussion and conclusions section.

2. Problem Description

In this section, we outline the problem setup in terms of governing equations, bulk constitutive model, interfacial friction law and initial stress field.

2.1. Boundary value problem

The governing equations for the boundary value problem are as follows (see also Table 1 for parameter definitions):

$$\nabla \cdot \sigma = \rho \ddot{u} \quad in \quad V \tag{1a}$$

$$\sigma \cdot n = T \quad on \quad S_T \tag{1b}$$

$$u = u_o \quad on \quad S_u \tag{1c}$$

$$T^{f+} + T^{f-} = 0 \quad on \quad S_f \tag{1d}$$

The balance of linear momentum is solved in the bulk V. We neglect body forces (e.g. gravity or those arising from pore fluids). The traction boundary condition and displacement boundary condition are specified on S_T and S_u, respectively. Along the fault interface S_f, the positive side fault interface traction T^{f^+} and the negative side fault interface traction T^{f^-} are governed by the traction at split node algorithm proposed by (Day et al., 2005). The initial values of the fault normal and shear stresses are computed by projecting the initial stress tensor on the fault surface. The rupture is initiated by including a perturbation shear stress term with a value $\Delta\tau$ in the initial conditions over a finite length along the fault interface in addition to the initial stress state τ_o. The detailed implementation strategy is covered in the numerical implementation section. We restrict this study to small strain kinematics.

Table 1: Parameters Description (Section 2.1)

Parameter	**Symbol**	**Parameter**	**Symbol**
Bulk domain	V	Traction boundary	S_T
Displacement boundary	S_u	Interface boundary	S_f
Cauchy stress tensor	σ	Initial stress tensor	σ_o
Stress perturbation tensor	$\Delta\sigma$	Normal vector	n
Exterior traction value	T	Interface traction	$T^{f^+}T^{f^-}$
Displacement, Acceleration vector	u, $\ddot{u}$	Exterior displacement	u_o

2.2. Damage-breakage rheology model

The continuum damage-breakage (CDB) rheology model provides relations between displacement gradients and stresses complementary to the equation set (1), which is necessary for the closure of the system of equations. Here we provide a general overview of the CDB model, and refer to earlier papers: (Lyakhovsky et al., 2011; Lyakhovsky and Ben-Zion, 2014a,b; Lyakhovsky et al., 2016) for detailed derivations and discussions. Table 2 summarizes the parameter choice in this study.

The CDB rheology model combines aspects of a continuum viscoelastic damage framework for brittle solid with a continuum breakage mechanics for granular flow within dynamically generated slip zones. This is accomplished by defining a scalar damage parameter (α) which accounts for the density of distributed cracking (Lyakhovsky et al., 1997), together with a scalar breakage parameter (B) representing grain size distribution of a granular phase (Einav, 2007a,b). Both parameters are defined within the range of $[0, 1]$.

The starting point is to formulate the free energy of the deforming medium and include appropriate modifications to account for the damage-breakage effects. To that end, the free energy F is developed as a function of elastic strain ϵ^e, damage parameter α, its spatial gradient $\nabla\alpha$, and the breakage parameter B. The gradient term accounts for the effects of spatially heterogeneous damage in regions around each point (Bazant and Jirásek, 2002) and prevents damage localization in bands of null thickness with vanishing energy dissipation in the quasi-static limit. Thus, it provides an intrinsic length scale for non local damage evolution that is resolvable with sufficient mesh refinement. Following (Lyakhovsky and Ben-Zion, 2014b), the free energy is partitioned by the breakage parameter B into a solid phase ($B = 0$), a granular phase ($B = 1$) or a mixture of both phases ($0 < B < 1$) (please refer to Appendix A.1 for a graphical representation):

$$F(\epsilon^e, \alpha, \nabla\alpha, B) = (1 - B)F_s(\epsilon^e, \alpha, \nabla\alpha) + BF_b(\epsilon^e) \tag{2}$$

The free energy for the solid phase F_s, and the free energy for the granular phase F_b in equation (2) are given by:

$$F_s(\epsilon^e, \alpha, \nabla\alpha) = \frac{1}{\rho}(\frac{\lambda}{2}I_1^2 + \mu I_2 - \gamma I_1\sqrt{I_2} + \frac{\nu}{2}\nabla_i\alpha \cdot \nabla_i\alpha) \tag{3}$$

$$F_b(\epsilon^e) = \frac{1}{\rho}(a_o I_2 + a_1 I_1\sqrt{I_2} + a_2 I_2^2 + a_3\frac{I_1^3}{\sqrt{I_2}}) \tag{4}$$

where the mass density ρ, first Lamé constant λ and shear modulus μ are rock properties. As a first order approximation, ρ and $\lambda = \lambda_o$ are kept constant during the deformation, but the shear modulus μ evolves with damage (see equation (7) given below). The coefficient ν presented in equation (3) introduces a non-local contribution in the stress tensor through the damage gradient. Here, we neglect the damage gradient to focus on on the local damage rheology and set $\nu = 0$. For the fully dynamic problem considered here, localization bands are still resolvable with sufficient mesh refinement. The problem remains well-posed due to the interplay of inertia effects and effective damage viscosity which introduces a length scale of the order of $c\tau$, where c is the characteristic wave speed and τ is the viscous relaxation time scale (Needleman, 1988).

$I_1 = \epsilon_{ij}^e\delta_{ij}, I_2 = \epsilon_{ij}^e\epsilon_{ij}^e(i, j = 1, 2, 3)$ are the first and second invariants of elastic strain ϵ^e. a_o, a_1, a_2, a_3 are coefficients of granular phase energy (see (Lyakhovsky and Ben-Zion, 2014a) for detailed derivation). By taking derivative of equations (3) and (4) with respect to elastic strain ϵ^e_{ij}, we obtain stress tensor in the two phases separately (See also (Lyakhovsky and Ben-Zion, 2014b)):

$$\sigma_{s,ij} = (\lambda - \frac{\gamma}{\xi})I_1\delta_{ij} + (2\mu - \gamma\xi)\epsilon^e_{ij} - \nu\nabla_i\alpha\nabla_j\alpha \quad (5)$$

$$\sigma_{b,ij} = (2a_2 + \frac{a_1}{\xi} + 3a_3\xi)I_1\delta_{ij} + (2a_0 + a_1\xi - a_3\xi^3)\epsilon^e_{ij} \quad (6)$$

The strain invariant ratio is defined as $\xi = I_1/\sqrt{I_2}$. In the general 3D case, ξ spans values from $-\sqrt{3}$ (isotropic compression) to $\sqrt{3}$ (isotropic tension). The damage variable α ranges from 0 (intact material) to 1 (fully damaged material). Increasing α reduces the shear modulus μ and increases the damage modulus γ, as given by the following equations (see also (Lyakhovsky and Ben-Zion, 2014b)):

$$\mu = \mu_o + \alpha\xi_o\gamma_r \quad (7)$$

$$\gamma = \alpha\gamma_r \quad (8)$$

where μ_o denotes the initial shear modulus and γ_r is the damage modulus when the damage variable reaches its maximum ($\alpha = 1$). ξ_o is the strain invariant ratio at the onset of damage, which is considered as a material property related to the internal friction angle (see equation (A.1)). For Westerly granite, the ξ_o ranges from -0.7 to -1 (Lyakhovsky et al., 1997). We assume the Poisson ratio to be 0.25 which is appropriate for most rock types.

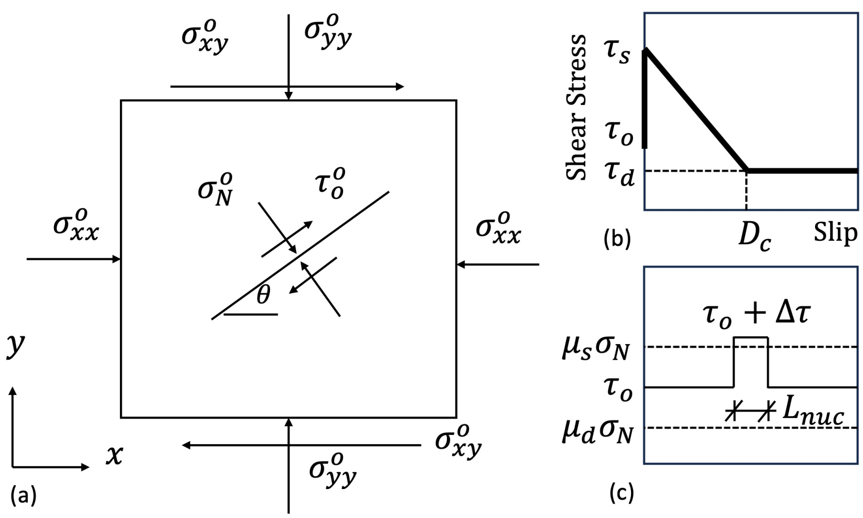

Figure 1: **Problem Description. (a) The background initial stress field ($\sigma^o_{xx}, \sigma^o_{yy}, \tau^o_{xy}$) and the fault local stress field (σ_N, τ_o). Different faults in the medium may have different orientations θ, and thus each fault may sustain different local normal stress and shear stress. (b) The linear slip weakening friction law connecting shear stress and slip along fault interfaces. The initial shear stress is labeled as τ_o, if the resolved shear stress τ is below the value of frictional strength τ_s, the fault interfaces remain locked with zero slip. After τ reaches the frictional strength, the strength linearly decreases over a critical slip distance D_c, and reaches its residual value τ_d. (c) A schematic of shear stress and strength distribution along the fault as well as the nucleation process by overstressing. The vertical axis shows relative values of initial shear stress τ_o, peak shear strength $\mu_s\sigma_N$ and residual shear strength $\mu_d\sigma_N$. The overstressing region has a length L_{nuc} and overstress value $\tau_o + \Delta\tau$, which slightly exceeds the peak shear strength.**

Following (Lyakhovsky and Ben-Zion, 2014a,b), the flow rule for the permanent strain ϵ^p is given by:

$$\frac{d\epsilon^p_{ij}}{dt} = C_g B^{m_1}\tau^{m_2}_{ij} + A\tau^n_{ij}exp(-\frac{Q}{RT}) \quad (9)$$

The first term on the right side represents the contribution of breakage to the inelastic deformation while the second term represents the contribution of thermally activated processes. Here, C_g is a tunable material parameter the controls the rate of permanent strain accumulation due to breakage, $\tau_{ij} = \sigma_{ij} - 1/3\sigma_{kk}\delta_{ij}$ is the deviatoric stress tensor, and m_1, m_2 are tunable power constants; the Newtonian-like granular flow is only realized as $B \approx 1$ with relatively high m_1 value and $m_2 = 1$ (Lyakhovsky and Ben-Zion, 2014a,b). A and n are empirical constants, Q is activation energy, T is temperature. The second term reflects the fact that increasing the temperature promotes flow and the accumulation of permanent strain even at low values of the breakage variable (B). Here, we restrict our focus to breakage-driven permanent strain growth and neglect the temperature dependence. Temperature effects may become important, though, with depth or if shear heating is considered. Further discussion is included in Section 4.

The evolution equations for damage (α) and breakage (B) parameters are given by (see (Lyakhovsky et al., 2011) for detailed derivation):

$$\frac{\partial \alpha}{\partial t}\begin{cases}(1-B)[C_d I_2(\xi-\xi_o)+D\nabla^2\alpha], & \xi \geq \xi_o \\ (1-B)[C_1 exp(\frac{\alpha}{C_2}) I_2(\xi-\xi_o)+D\nabla^2\alpha], & \xi < \xi_o\end{cases} \tag{10}$$

$$\frac{\partial B}{\partial t}\begin{cases}C_B P(\alpha)(1-B) I_2(\xi-\xi_o), & \xi \geq \xi_o \\ C_{BH} I_2(\xi-\xi_o), & \xi < \xi_o\end{cases} \tag{11}$$

In equation (10), the parameter C_d controls the rate of damage accumulation. D is a damage diffusion coefficient. As discussed earlier, we restrict our focus in this study to a local model neglecting non-local effects. That is, we set $D = 0$. With the adopted formulation, permanent strain begins to rapidly accumulate near the transition to the granular phase. This is different from earlier formulations (Hamiel et al., 2004; Xu et al., 2015) in which plastic strain also accumulated in the process of damage increase ($\xi \geq \xi_o$). The healing rate of damage variable α is governed by an exponential function with coefficients C_1 and C_2. As for the breakage evolution shown in equation (11), the parameter C_B is assumed to be related to C_d. Here we adopt $C_B = 10C_d$ as suggested in (Lyakhovsky and Ben-Zion, 2014a,b). The probability function $P(\alpha)$ in the breakage parameter evolution equation (11) controls the timing for transition to the granular phase, such that the transition happens only when damage reaches its critical value α_{cr} (see also Appendix equation (A.3), (Lyakhovsky and Ben-Zion, 2014b) for derivation of α_{cr}). As pointed out in (Lyakhovsky and Ben-Zion, 2014b), the coefficient controlling the breakage healing is not well constrained. Some experiments suggest that the granular flow may abruptly halt under low velocity. Here we set $C_{BH} = 10^4\ 1/s$ in equation (11), as suggested in (Lyakhovsky et al., 2016).

2.3. Linear slip weakening friction law

In this study, the slip behavior of fault interfaces is assumed to be governed by a linear slip weakening friction law illustrated in Fig.1(b). The frictional strength is given by the product of the normal stress on the fault and the friction coefficient. Before the resolved shear stress τ reaches the peak strength $\tau_s = \mu_s\sigma_n$, the fault is stuck with zero slip. After τ reaches τ_s, the frictional strength decreases to a residual strength $\tau_d = \mu_d\sigma_n$ value over a critical distance D_c and the fault slips following the frictional strength evolution. The drop in friction coefficient from μ_s to μ_d is linear. For slip values larger than D_c, the dynamic friction coefficient μ_d remains constant. We note that the coupling between frictional sliding on the fault and asymmetric damage in the bulk may lead to transient changes in the fault normal traction. A regularization of the friction law, in which the instantaneous frictional strength depends on the history of the normal stress rather than the instantaneous normal stress value, may be needed if the normal stress changes abruptly, as shown by (Cochard and Rice, 2000). For the damage related problem considered here, an intrinsic regularization emerges from the finite time scale of the damage variable α evolution which leads to gradual, rather than instantaneous, changes in the normal stress.

2.4. Numerical implementation

We developed an app, called MOOSE-FARMS `https://github.com/chunhuizhao478/farms`, as a dynamic rupture simulator based on the Multiphysics Object-Oriented Simulation Environment (MOOSE) (Lindsay et al., 2022), an open source massively parallel finite element code from the Idaho National Lab (INL). MOOSE-FARMS simulates dynamic rupture propagation on frictional interfaces using the cohesive zone model approach. It includes options for both linear slip weakening and rate and state friction laws, handles complex fault geometries (Abdelmeguid et al., 2023), and accepts different types of bulk rheology. In this study, we extended MOOSE-FARMS to include an implementation for the continuum damage-breakage model. We combine this extension with the linear slip weakening friction law to simulate dynamic rupture propagation in complex fault zones with off-fault damage and phase transition to granular flow.

To create fault interfaces, we use MOOSE framework mesh generator `BreakMeshByBlockGenerator`, which breaks the interface and assign duplicate nodes to the newly-created surfaces. The methodology is explained in (Nguyen, 2014) in detail. Specifically for handling the fault network as will be discussed in section 3.2, the intersection point of fault network is duplicated with the total size equals to number of faults connecting at this node. Thus each fault is free to slip if activated.

We use explicit central difference to discretize in time and adopt Lysmer dampers to reduce the wave reflections on the boundaries S_u (Lysmer and Kuhlemeyer, 1969; Veeraraghavan et al., 2021). We apply far-field background initial stress field $(\sigma^o_{xx}, \sigma^o_{xy}, \sigma^o_{yy})$, see Fig.1(a). The sign convention is adopted to be positive for tension and clockwise shear. The values are specified in Table 2. The pre-existing faults inside the simulation domain experience various local stress fields (σ_N, τ_o) depending on their orientation (θ).

The nucleation is incorporated by overstressing $\Delta\tau$ in addition to initial stress field τ_o along a section of the fault S_f with a length L_{nuc} approximately equals to the elasto-frictional length scale $L_{fric} = \mu D_c/(\sigma_N(\mu_s - \mu_d))$ (Palmer and Rice, 1973; Ida, 1972), see Fig.1(c) for illustration. Here μ_{app} is the apparent friction, defined as the ratio of local shear τ to normal stress σ_N. The mesh size Δx is chosen to fully resolve the L_{fric} using at least $7 \sim 8$ elements, and the time step is constrained by the CFL condition. Table 2 summarizes the assumed properties.

Table 2: Parameters Description (Section 2.2-2.4)

Thermodynamics state variable	**Symbol**	**Value**	**Reference**
Damage Parameter	α	$[0, 1]$	
Breakage Parameter	B	$[0, 1]$	
Material Properties			
Density (kg/m^3)	ρ	2670	
First Lamé constant (GPa)	λ_o	32.04	
Initial shear modulus (GPa)	μ_o	32.04	
Damaged modulus at maximum damage (GPa)	γ_r	37.15	Computed following (Lyakhovsky and Ben-Zion, 2014a)
Coefficients of granular phase free energy (GPa)	a_0, a_1, a_2, a_3	$a_0 = 7.4289$ $a_1 = -22.14$ $a_2 = 20.929$ $a_3 = -6.067$	Computed following (Lyakhovsky and Ben-Zion, 2014a)
Kinematic of Damage-Breakage			
Strain invariant ratio at onset of damage	ξ_o	-0.8	equation (A.1), the frictional angle is 46.8°
Strain invariant ratio at transition			

Continued on next page

Table 2 – Continued from previous page

	Symbol	Value	Reference
between solid and granular phases	ξ_1	0.8248	Computed following (Lyakhovsky and Ben-Zion, 2014a), equation (A.2)
Strain invariant ratio at onset of breakage	ξ_d	-0.9	(Lyakhovsky et al., 2016) Table 1
Coefficient for damage accumulation rate (s^{-1})	C_d	Variable	Tunable parameter
Coefficient of damage healing (s^{-1})	C_1, C_2	300, 0.05	Tunable parameter, (Lyakhovsky et al., 2016), Table 1
Coefficient of breakage accumulation rate (s^{-1})	C_B	$= 10\ C_d$	Tunable parameter, (Lyakhovsky and Ben-Zion, 2014a), section 4.2. (Lyakhovsky and Ben-Zion, 2014b), Table 1
Coefficient of breakage healing rate (s^{-1})	C_{BH}	10^4	Tunable parameter, (Lyakhovsky et al., 2016), Table 1
Fluidity of granular flow ($Pa^{-1}\ s^{-1}$)	C_g	10^{-10}	Tunable parameter
Power index for granular flow	m_1, m_2	10, 1	Tunable parameter, (Lyakhovsky and Ben-Zion, 2014b), table 1, equation 18
Width of transition region	β	0.03	Tunable parameter, equation A5. (Lyakhovsky and Ben-Zion, 2014b), Table 1
Diffusion coefficient for damage accumulation (m^2/s)	D	0	
Coefficient of stress with non-local damage (MPa m^2)	ν	0	
linear slip weakening Friction			
Resolved local normal stress / shear stress	τ_o, σ_N	Variable	
Characteristic length scale (m)	D_c	0.4	(Harris et al., 2009)

Continued on next page

Table 2 – Continued from previous page

	Symbol	**Value**	**Reference**
Static friction coefficient	μ_s	0.677	
Dynamic friction coefficient	μ_d	0.1	
Peak frictional strength	τ_s	$= \sigma_N \mu_s$	
Residual frictional strength	τ_d	$= \sigma_N \mu_d$	
Initial Stress Field			
Initial far-field stress along xx direction (MPa)	σ^o_{xx}	-135	
Initial far-field stress along xy direction (MPa)	σ^o_{xy}	70	
Initial far-field stress along yy direction (MPa)	σ^o_{yy}	-120	
Problem specific setup: single planar fault			
Domain length (km)	L_x	30	
Domain length (km)	L_y	30	
Frictional length scale (m)	L_{fric}	185	
Nucleation patch size (m)	L_{nuc}	200	
Nucleation overstress (MPa)	$\Delta\sigma$	11.6	
Mesh size (m)	Δx	25	
Time step (s)	Δt	5×10^{-4}	
Problem specific setup: immature fault zone			
Domain length (km)	L_x	20	
Domain length (km)	L_y	20	
Frictional length scale (m)	L_{fric}	346	
Nucleation patch size (m)	L_{nuc}	400	
Nucleation overstress (MPa)	$\Delta\sigma$	18.2	
Adaptive Mesh size (network region) (m)	Δx	50	
Adaptive Mesh size (boundary region) (m)	Δx	200	
Time step (s)	Δt	2×10^{-4}	

3. Results

3.1. Single planar fault

To explore how the damage-breakage process influences dynamic rupture characteristics, we first consider a single right-lateral planar fault (see Fig.2(a)), similar to what was investigated previously by (Xu et al., 2015) but now with the expanded constitutive description that also accounts for transition into granular flow. The directions of maximum and minimum compression stresses are also highlighted. We nucleate the rupture at the center of the fault. As the rupture grows bilaterally, the slip causes asymmetric changes in the bulk mean stress. We denote the regions expected to have tensile or compressive mean stress perturbations by "T" and "C", respectively. The dynamic friction coefficient μ_d governing the stress drop is set to be $\mu_d = 0.1$, which facilitates a high dynamic stress drop. This promotes more damage especially when coupled with high enough damage evolution rate C_d. We set $C_d = 10^7\ 1/s$ in the simulations leading to Fig. 2-5. However, we also consider a range of C_d values (see Fig. 6) to evaluate the effect of damage rate on rupture characteristics and bulk evolution.

Velocity and Damage Fields: In Fig.2 (b)-(c), we visualize the particle velocity and the damage fields within $L_y = 3\ km$. Due to anti-symmetry, we just focus on the left half of the domain only where the rupture is propagating from right to left. As shown in Fig.2(b), we show several snapshots of particle velocity amplitudes. We note the emergence of shock-like wave features carried by the rupture tips. These are Mach cones, characteristic of supershear ruptures, which form when the rupture propagation speed exceeds the shear wave speed. Our choice to model a supershear rupture is motivated by the increased frequency of their occurence in large earthquakes (Dunham and Archuleta, 2004; Bao et al., 2019; Ren et al., 2024; Bao et al., 2022). In Appendix A.5 we discuss similar results for the case of sub-Rayleigh rupture.

On the tensile side ("T") of the fault where damage accumulates, the Mach front becomes more diffuse and the peak velocity carried by it clearly lower in magnitude than the velocities carried by the shock front on the compressive side ("C"). However, the diffuse velocity field behind the Mach cone on the tensile side ("T") of the fault exhibits a relatively higher magnitude over a larger region compared to the compressive side ("C"), in which the Mach front is sharper and the high amplitude of the velocity field is localized in a narrow region behind the rupture tip. In Appendix A.3, we further compare the main features of the velocity field from a rupture propagating in a solid governed by the continuum damage-breakage model versus a rupture in a linear elastic medium. In Appendix A.6, we also outlined time history evolution of slip rate, shear stress and normal stress at location 1km, 3km, 5km, 7km away from the center, which further explains how damage perturbs the associated fields during a dynamic rupture event.

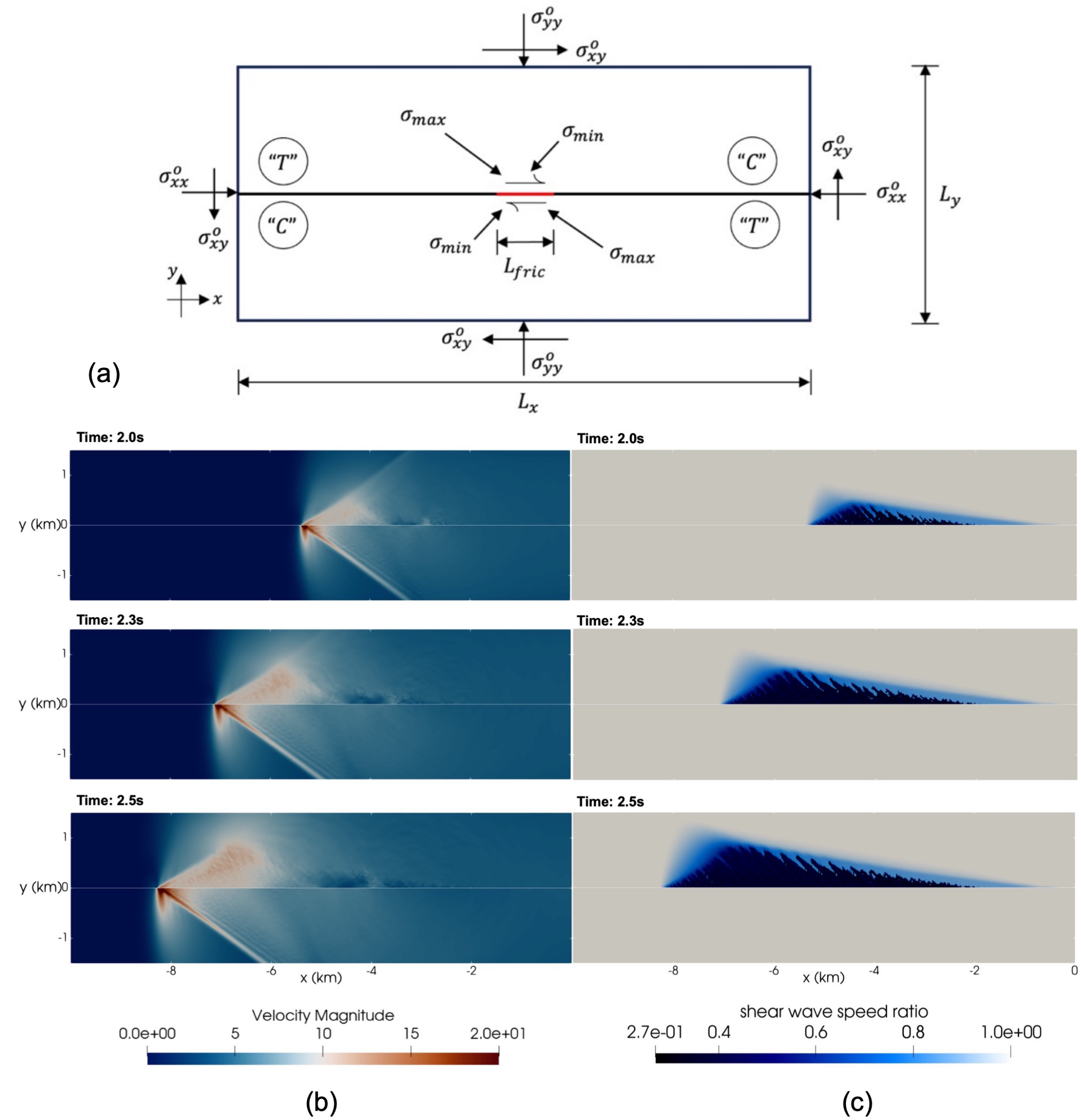

Figure 2: **The Planar fault case. (a) Geometry setup. The nucleation patch is marked in red. The rupture involves right-lateral slip and the principal stress directions are shown by arrows. The compressional and tensile sides are depicted using the symbols "C" and "T", respectively. (b) Selected snapshots for particle velocity magnitude showing a clear signature of Mach cones associated with supershear rupture propagation. Note the asymmetry in the particle velocity distribution due to the preferential damage accumulation on the tensile side of the rupture (upper half of the figure) compared to the compressive side (lower half of the figure), which is due to the damage on the tensile side. (c) Selected snapshots for shear wave speed ratio. Due to anti-symmetry, we restrict our focus on the left half of the domain only where the rupture propagates from right to left. We observe a distributed fan-shape damage profile with localized damage bands buried inside and it is emerging from the fault.**

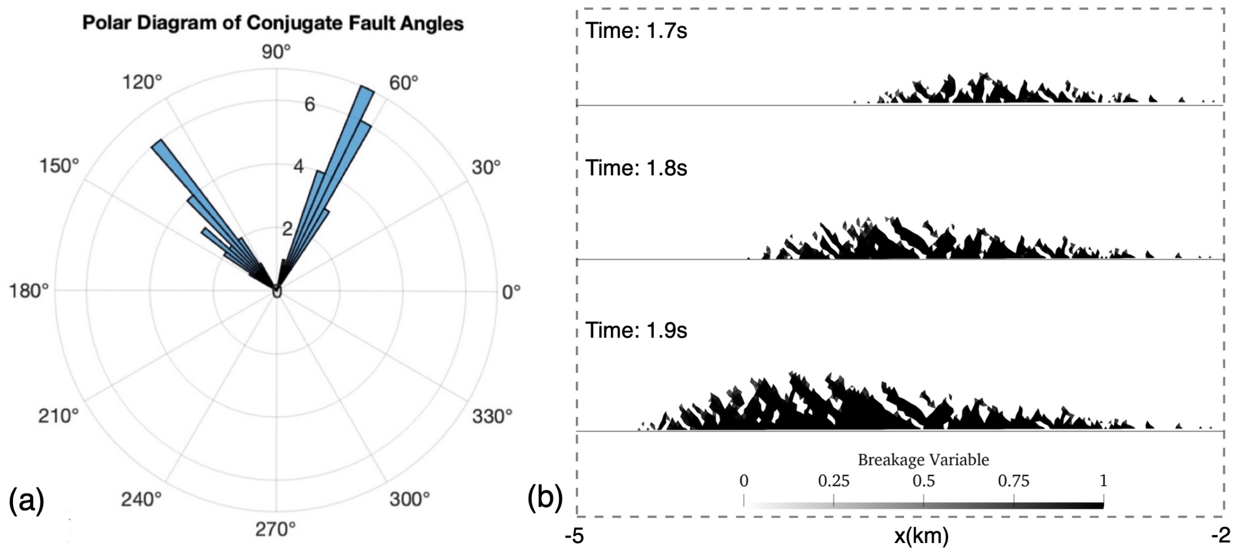

Figure 3: **The Planar fault case. (a) Polar diagram showing representative angles of newly-formed conjugate branches measured counter-clockwise with respect to the x direction; the measurements of representative damage band angles are taken place at early onset of damage bands accumulation period (1.7s $\sim$ 1.9s). (b) Selected extraction snapshots for breakage damage bands. We observe clear conjugate band feature with growth of band width as time progresses.**

Fig.2(c) shows time snapshots of off-fault damage accumulation, represented by shear wave speed ratio. The shear wave speed ratio is given by $\sqrt{\mu/\rho}/c_s^o$, where c_s^o is the initial shear wave speed for intact material. As damage accumulates, the shear modulus decreases and the shear wave speed is reduced. From Fig.2(c), we observe a fan-shaped distributed damage profile which qualitatively agrees with ones observed in (Xu et al., 2015). The place where the damage starts to accumulate is determined by the strain invariant ratio threshold ξ_o and the local strain state (represented by strain invariant ratio ξ) associated with the rupture tip. The main difference compared with (Xu et al., 2015) is the transition into granular phase near the rupture front and the emergence of conjugate bands (shown by the darker blue shades in Fig.2(d)). This burst of granular localization takes place when the damage α reaches its critical value α_{cr}. The formation of the conjugate bands is consistent with expectations of yielding in pressure-sensitive quasi-brittle solids. The orientation of these bands is controlled by the angle of internal friction and the local direction of the maximum principal stress. We observe the leftwards bands possess longer lengths at later time and overshadow the rightwards ones in Fig.2(c), the measurement of conjugate bands angles is thus performed in the early times (see Fig.3) as will be explained in the next subsection.

Co-evolution of Damage and Stress Fields: A polar diagram (see Fig.3(a)) shows the frequencies of two favorable band orientations with respect to the x axis. These measurements are sampled from the rupture history between 1.7s and 1.9s. In Fig.3(b) we show time snapshots of damage bands, represented by breakage variable (B) distribution. From the polar diagram (see Fig.3(a)), we conclude the average angles for two conjugate bands are about 65.1° and 133.9° (positive angle is measured counterclockwise from the positive x-axis). These angles appear to be inconsistent with the orientation of the initial stress field. However, considerations of the dynamic nature of the rupture and the co-seismic evolution of the material properties due to damage resolve this contradiction.

Specifically, while the maximum principal compression is initially oriented at $\psi = 135^o$ with respect to the fault plane, this orientation locally changes near the fault as the rupture expands and accelerates. We observe that the maximum principal compression becomes close to vertical $\psi \sim 95^o$ in the near fault region behind the rupture tip after the transition into supershear propagation (see also Appendix A.4). This dynamic rotation is consistent with reports in earlier studies (Poliakov et al., 2002; Rice et al., 2005; Rousseau and Rosakis, 2009), but is further exacerbated here due to the co-seismic changes in the elastic properties as a result of damage accumulation. The dynamic orientation of the maximum principal compression approximately bisects the conjugate band as expected from theories of strain localization in inelastic materials

(Rudnicki and Rice, 1975). The average angle between the conjugated bands is approximately 68.8°. We note that the initial angle of internal friction based on the choice of the ξ_o parameter in our CDB model is about $\phi = 46.8^o$. See also Table 2 which yields an estimate for the angle between the bands at the onset of localization to be approximately $90 - \phi = 43.2^o$. The difference between the observed angle and the estimated one suggests that the effective angle of internal friction is decreasing with deformation to a mobilized value of $\sim 21.2^o$. The evolution of the effective angle of internal friction is an emergent property of the CDB model due to the post-peak softening response associated with the damage-breakage transition.

Complex off-fault failure patterns were also observed in the study of (Okubo et al., 2019), where off-fault fractures are discretized by unstructured mesh and each fracture plane is governed by mode I or mode II cohesive law. As the cohesion drops to zero, it is marked as a secondary-activated plane. The main difference in comparison with the current study is in the interpretation of distributed and localized damage profiles. In (Okubo et al., 2019), each generated fracture plane is a consequence of loss of cohesion at its plane due to stress perturbation generated by the main rupture. The off-fault damage bands appear locally first, with a path following mesh discretization, and the distributed behavior can then be interpreted as a cluster of damage bands. However, in the current approach, damage is a distributed behavior, which evolves as a function of strain invariant ratio ξ. Breakage or granular flow is associated with localized features that are only activated when damage reaches its critical level. In contrast to (Okubo et al., 2019), where a macroscopic damage profile is assembled by localized bands, here the highly damaged localized granular bands are generated within distributed damage. In (Okubo et al., 2019) the local fractures follow the mesh discretization, while in our model the damage-breakage emerge as continuum fields that are not directed by the mesh topology.

Damage vs Plasticity: It is also informative to compare the CDB model with off-fault plasticity results for dynamic rupture since both can be used to quantify off-fault damage mechanism and inelastic deformation accumulation. In order to explore some of the differences between the two rheologies, we perform the same single planar fault simulations with Drucker-Prager (DP) plasticity using our in-house code FEBE (Abdelmeguid and Elbanna, 2022a). We assume the same internal friction angle as derived above from the CDB model and zero cohesion. Fig.4(a) shows slip rate and slip along the fault for Drucker-Prager plasticity model up to 2.0 s (marked in blue), while Fig.4(b) shows corresponding results for the CDB model (marked in red. The curves in Fig.4(a) and Fig.4(b) are plotted every 0.1 s. The results indicate higher peak slip rate and slip, as well as faster propagation velocity, in the continuum damage-breakage model case compared to the Drucker-Prager model.

Furthermore, the oscillations observed in the slip rate profile behind the rupture tips in the case of the CDB model are attributed to the accumulation of damage and changes in the elastic moduli and normal stress, with reflection and diffraction of elastic waves within the fault zone. In contrast, the slip rate and slip lines for the DP case are smoother and lack these oscillations because the elastic properties remain constant.

We also evaluate the plastic work $W = \int_\Omega \sigma \dot{\epsilon}_p d\Omega$ for both models, where σ is the total stress. The plastic work (see Fig.4(c)) inferred from the Drucker-Prager model up to 2.0 s equals $12.2639 \times 10^4\ MN \cdot m$. This is higher than what is inferred for the continuum damage-breakage model $3.3681 \times 10^4\ MN \cdot m$. This result, together with the larger slip, slip rate, and rupture speed which characterize the rupture in the CDB model, suggest that off-fault damage-breakage facilitate higher seismic energy radiation and lower dissipation than a rupture propagating in an elastoplastic bulk with constant elastic moduli.

In Fig.5, we present results with a focus on shear wave speed ratio (Fig.5(a)-5(b)) and equivalent inelastic strain (Fig.5(c)-5(d)). As shown in Fig.5(a)-5(b), the shear modulus, and consequently the shear wave speed, degrade in the continuum damage-breakage model, whereas in the plasticity model the wave speed remains constant. In Fig.5(c)-5(d) we compare the distributions of equivalent inelastic strain. Recall that the equivalent inelastic strain rate is given by $\dot{\gamma}_{eq} = \sqrt{2\dot{\epsilon}^p \dot{\epsilon}^p}$, where ϵ^p is the plastic strain in Drucker-Prager or the permanent strain in the granular phase in CDB model. Several findings can be drawn from the comparison: (1) The width of the inelastic zone is different; it is narrower in the CDB model compared to the DP model (Fig.5(c)-5(d)). However, the extent of the region experiencing damage in the CDB model, encompassing both the solid and the granular phases, is comparable to the extent of plastic strain accumulation in the DP case (see Fig.5(b)-5(c)). (2) The shape and magnitude of inelastic strain distribution is different in the two cases. The Drucker-Prager plasticity exhibits a distributed fan-like pattern. The magnitude of inelastic strain has higher values close to the fault and decreases gradually into the far-field media. On the other hand, the inelastic strain of the CDB model is narrower and essentially a byproduct of granular phase transition. It is a localization feature favored by post-peak rheological softening, as seen in Fig.2(d) and Fig.5(b). The width of the zone of inelastic strain increases in both cases as rupture expands bilaterally consistent with what is expected for a crack-like rupture. This evidently occurs in a weaker form with the CDB rheology, suggesting a less smooth rupture propagation than with DP plasticity.

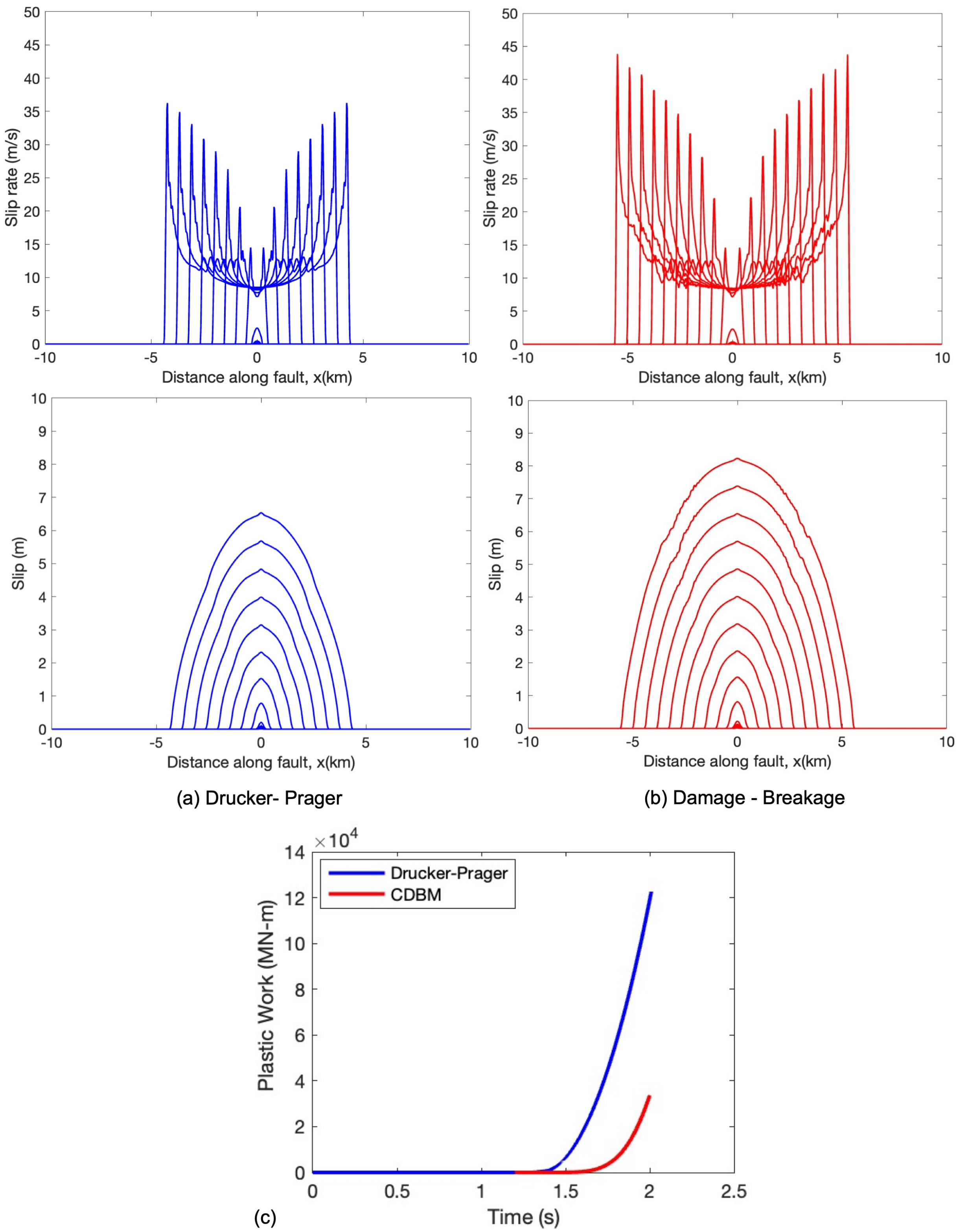

Figure 4: **Comparison of rupture characteristics emerging from the continuum damage-breakage model and the Drucker-Prager plasticity model for the planar fault case. The same setup shown in Fig.2(a) is used in this comparison. (a) Slip rate and slip profiles along the fault for Drucker-Prager plasticity. (b) Slip rate and slip profiles along the fault for the CDB model. The lines are plotted every $0.1\ s$ up to $t = 2.0\ s$ for both models. (c) Plastic work accumulation as a function of time for the Drucker-Prager plasticity (blue curve) and the continuum Damage-Breakage Model (red curve).**

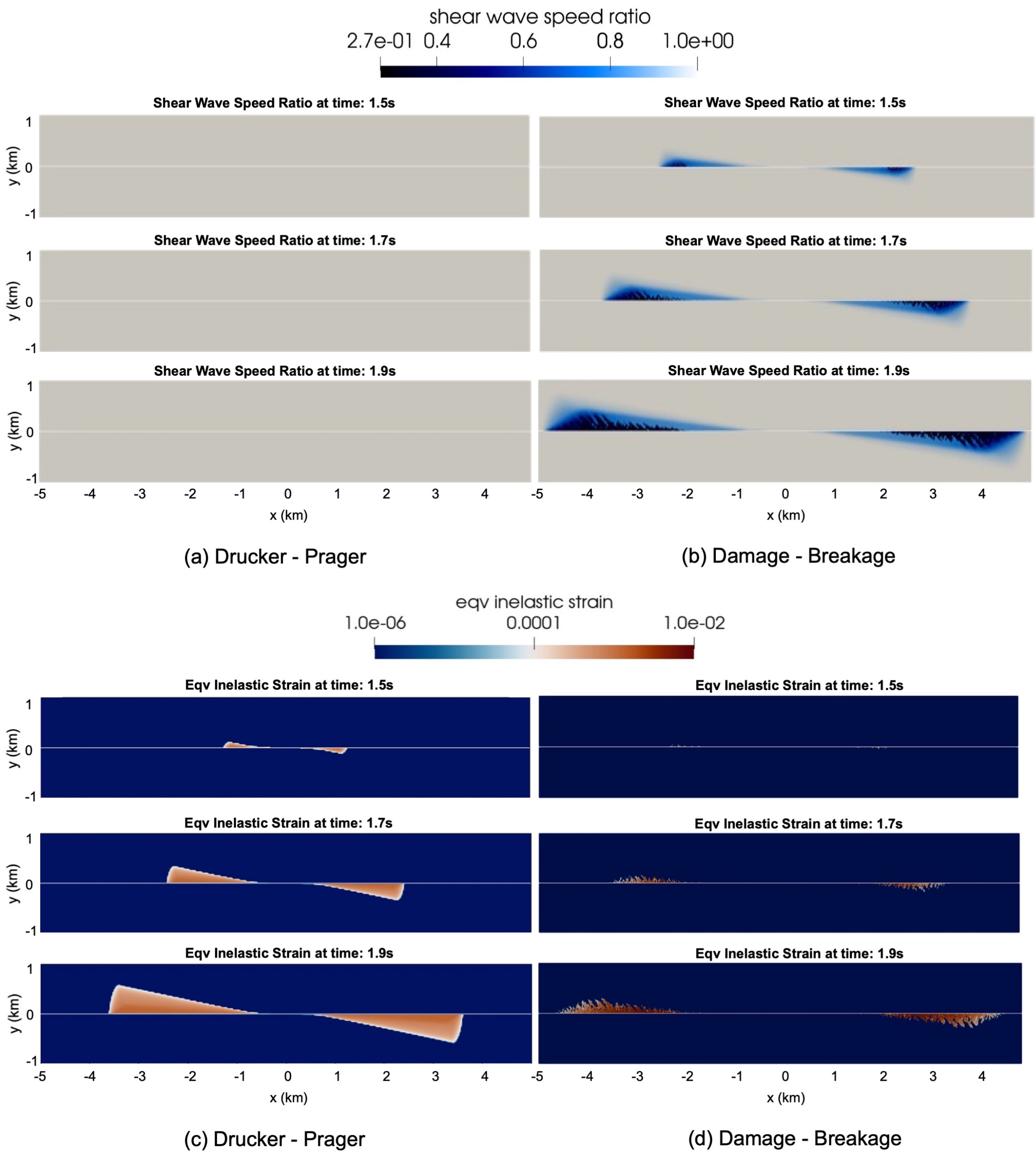

Figure 5: **Comparison of bulk properties between the continuum damage-breakage model and the Drucker-Prager plasticity for dynamic rupture simulations. The same problem setup shown in Fig.2(a) is used in this comparison. (a) & (b) Selected snapshots for the instantaneous shear wave speed ratios in the two models (column a is Drucker-Prager plasticity, column b is for CDB model). The shear wave speed ratio remains equal to 1 for the DP model but it evolves in the CDB model. (c) & (d) Selected snapshots comparing the evolution of the equivalent plastic strain in the bulk simulated for the two models (column c is for Drucker-Prager plasticity, column d is for CDB model).**

Effect of Damage Accumulation Rate: To explore how the choice of C_d values affects the observed distributed damage or localized granular flow, we conduct a parametric study testing three additional cases, including $C_d = 10^4\ 1/s, C_d = 10^5\ 1/s$ and $C_d = 10^6\ 1/s$. We extend the geometry in Fig.2(a) along x direction $L_x = 60\ km$ and keep other parameters the same. Fig.6 shows the shear wave speed ratio corresponding to the cases $C_d = 10^4\ 1/s$, $C_d = 10^5\ 1/s$, $C_d = 10^6\ 1/s$, respectively. Recalling the results presented in Fig.2(d) for $C_d = 10^7\ 1/s$, several observations follow: (1) The C_d value controls the degree of damage and the timing for transition to granular flow (since we assume $C_B = 10\ C_d$). For example, for the $C_d = 10^5\ 1/s$ case, only mild distributed damage is observed, up to $25km$, without generating any localization, while $C_d = 10^7\ 1/s$ leads to extreme damage and rapid granulation in a relatively short time. The reduction in the shear wave speed is about 1% in the case of $C_d = 10^4\ 1/s$ and it increases to 8% for $C_d = 10^5\ 1/s$. Higher values of C_d leads to larger reduction in the shear wave speed. (2) In Fig.6(c), with $C_d = 10^6\ 1/s$, we observe the emergence of localization bands associated with breakage transition. However, as the rupture moves further away, the localized bands start to partially heal following equations (10) (11). As the unloading takes place behind the rupture tip, the strain invariant ratio decreases. Once it is smaller than the onset of damage value ξ_o, the granular flow could halt or even heal. However, this feature is mostly shadowed in the $C_d = 10^7\ 1/s$ case.

3.2. Fracture corridor as immature fault zone

We next study dynamic rupture propagation in a fault network where a cluster of faults may be present as typically observed in immature fault zones or in shallow regions that are relevant for many geo-energy applications. The fault network consists of multiple intersecting faults, each of which is 600 m long. The topology is similar to the one first used by (Xu and Needleman, 1994) to simulate complex dynamic fracture patterns, except that here each fault (or fracture) is resolved by at least 10 elements. At $t = 0\ s$, all faults are inactive due to our choice of the background stress and frictional parameters which ensure that the ratio of the locally resolved shear to noraml stress on each fault is smaller than the static coefficient of friction μ_s (see Table 2). We then initiate a rupture cascade by locally overstressing one of the faults (red line in Fig.7(a)) beyond its initial stress state. As the rupture propagates on this fault, the stress redistribution facilitated by the wave dynamics trigger other, initially inactive, faults. This is further enhanced by the damage-breakage processes which channel stresses and focus waves along additional directions that experience reduction in their elastic modulii. Eventually ruptures take place on most of the faults.

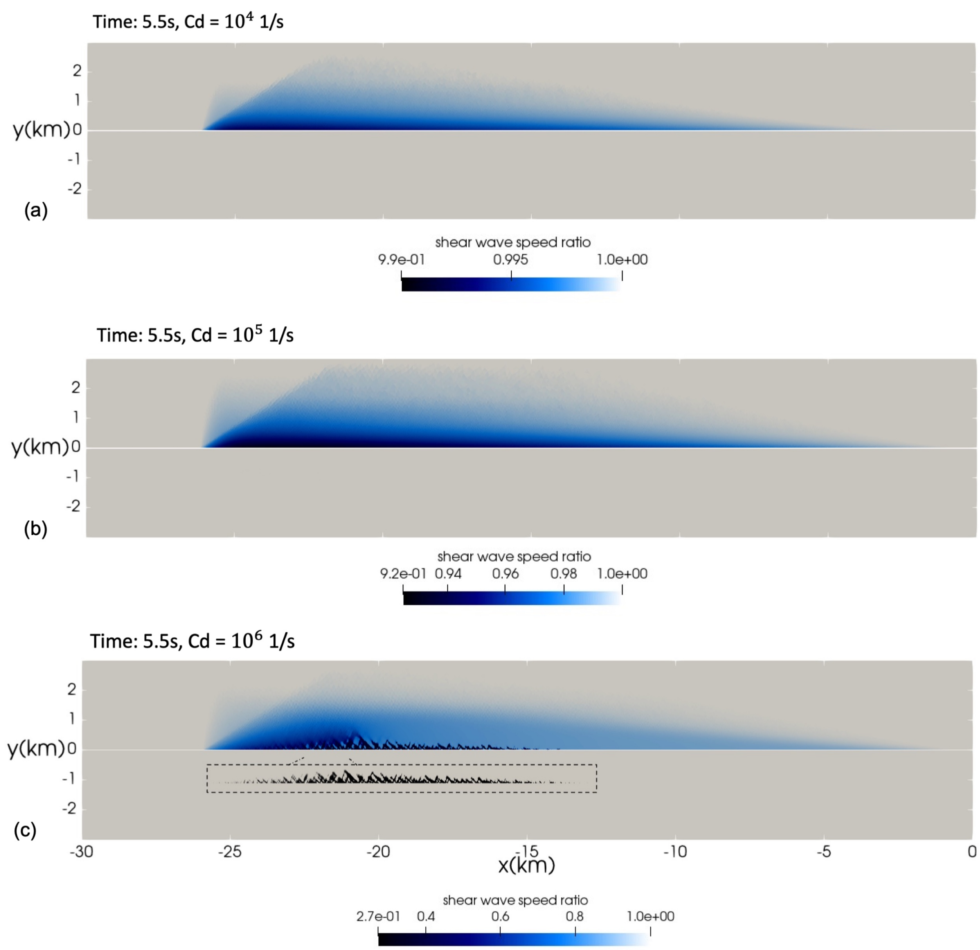

Figure 6: **The effect of the damage evolution rate C_d on the dynamic rupture propagation. We extend the geometry in Fig.2(a) such that $L_x = 60\ km$ and test the $C_d = 10^4\ 1/s$, $C_d = 10^5\ 1/s$ and $C_d = 10^6\ 1/s$ cases. (a) The $C_d = 10^4\ 1/s$ case. Only up to 1% reduction in the shear wave speed is observed at that particular time. (b) The $C_d = 10^5\ 1/s$ case. Up to 10% reduction in the shear wave speed is observed at that particular time. However, no breakage is observed. (c) The $C_d = 10^6\ 1/s$ case. The reduction in the shear wave speed is much higher (about 70%). Breakage bands are observed signaling transition to granular flow. The breakage generates at the front tip and halts/recovers as the tip gets far. The breakage profile is highlighted within a dash black box, see the text for detailed explanation.**

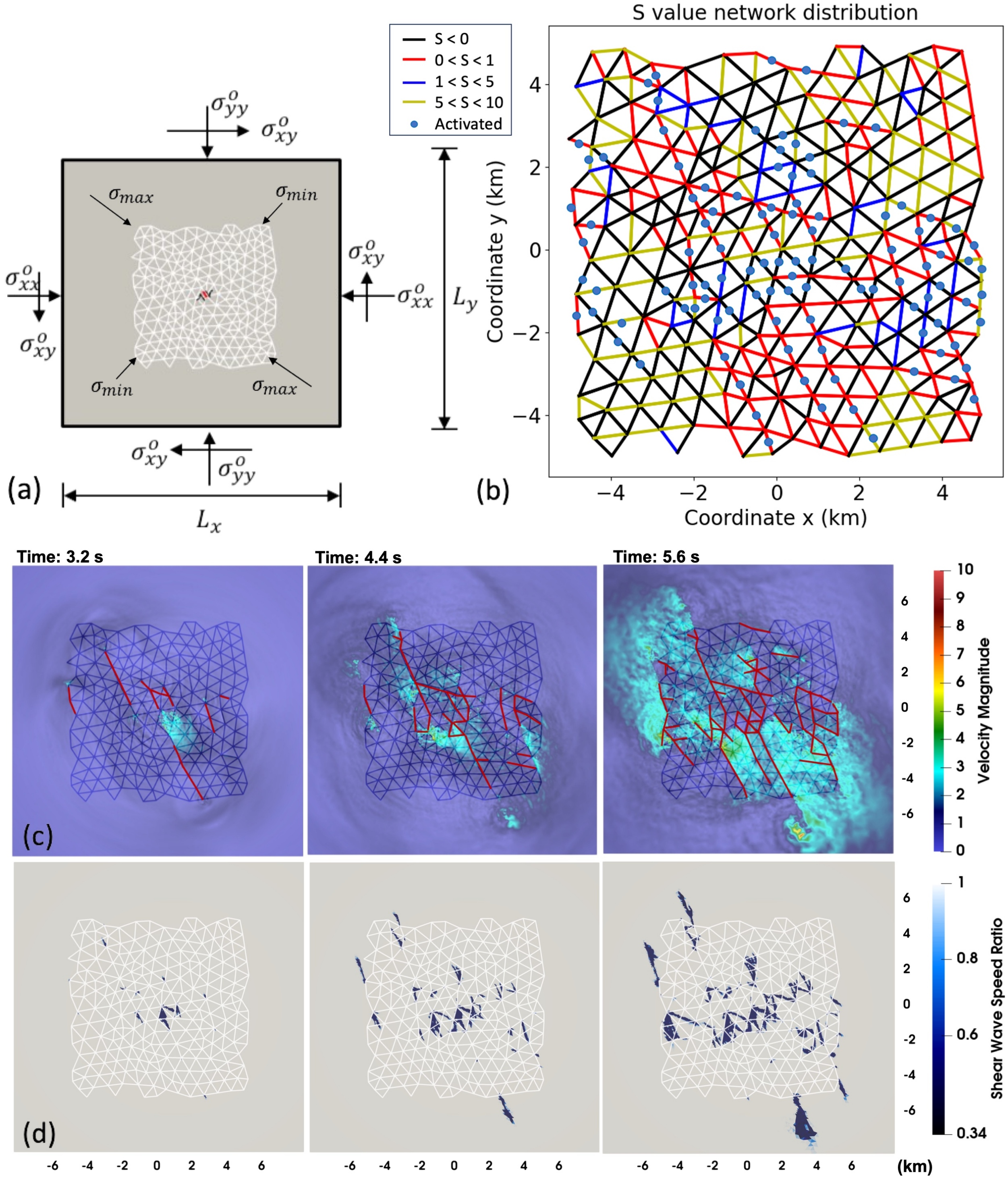

Figure 7: **The Fault network case. (a) Geometry setup. (b) The strength parameter S distribution for the network fault segments. We label all faults with $S < 0$ as dashed black color (where $\mu < \mu_d$), and use red, blue, yellow color lines to categorize cases $0 < S < 1$, $1 < S < 5$, $S > 5$, respectively. We place blue dots on each fault that is activelly slipping at time 5.6s (See (c)) as an example of the network state at a given instant of time. Most activated faults are within $0 < S < 1$ range. Note that for faults with initially $S < 0$, our choice of the background stress ensures that μ is initially less than μ_d. Thus, these faults are much harder to mobilize (c) Selected snapshots of the particle velocity magnitude. The activated faults are marked red.(d) Selected snapshots of shear wave speed ratio $C_d = 10^6\ 1/s$. Localized samage bands emerge from the corners and the fault intersection points. Please refer to the main text for further discussion**

Fig.7(a) illustrates the setup of the problem. We define the strength parameter $S = \frac{\mu_s - \mu}{\mu - \mu_d}$ (Das and Aki, 1977; Andrews, 1976) as a measure of how close the initial stress is to the static strength, where $\mu = \frac{\tau_S}{\sigma_N}$ is the apparent friction, computed from the ratio of the locally resolved shear stress and normal stress on each fault segment. The distribution of strength parameter S for network segments is shown in Fig.7(b). The source fault, marked in red in Fig.7(a), is activated by overstressing. It generates stress perturbations and destabilizes surrounding faults, which, in turn, produce subsequent nucleations and propagation of ruptures. As shown in Fig.7(c), the activated faults, marked in red, tend to connect and expand within the network as time progresses. Despite the complexity of the fault network activation, the distribution of the strength parameter, Fig.7(b), helps to understand the triggering sequence. Here we label the activated faults at time 5.6s with blue dots using 4 groups of the initial S parameter values: (1) $S < 0$ is shown with black color segments, where $\mu < \mu_d$, the faults are unable to nucleate spontaneously. (2) $0 < S < 1$ is marked as red color segments, where fast transition into super-shear rupture is expected. (3) $1 < S < 5$, where we may get a mix of sub-Rayleigh and supershear ruptures (blue color segments) (4) $S > 5$ are cases where rupture, if occurs, would be most likely sub-Rayleigh or where rupture will be blocked because of large static strength (yellow color segments). From Fig.7(b), we observe most of the faults activation to take place on $0 < S < 1$, approximately tracing the direction of those planes with optimal orientation with respect to the maximum principal stress, where the static strength is close to the initial stress state. This is consistent with the fact that for small S values, faults are more sensitive to stress perturbations and are easier to get activated. For large S parameter $S > 1$ or unfavorable $S < 0$ cases which get activated, the faults are located within the cluster of easily activated ($0 < S < 1$) ones. The activated faults with small S values promote the activation of the others by the strong enough stress perturbations carried by the wave field (Fig. 7(c)) as well as the stress redistribution due to damage accumulation (Fig.7(d)).

The distribution of off-fault damage, measured by the reduction in the shear wave speed, is shown in Fig.7(d). Comparing Fig.7(c) and Fig.7(d) indicates that regions with reduced shear wave speed largely exist within clusters of activated faults. This is not unexpected as we showed earlier for the single fault case. However, the damage pattern is also distinct in the sense that it does not necessarily follow the path of the red lines depicted in Fig.7(c). The damage is predominately localized and occasionally extends beyond the realm of activated faults reflecting a self-driven process. Specifically, the damage localization promotes fast phase transition into the granular phase, which causes further localization typically occurring at the nodes of the fault network and further growing from there. These junctions acts as barriers where further rupture propagation along a pre-existing segment is impeded. As the rupture is arrested, it releases a burst of seismic radiation and causes a strong stress concentration, damaging the surrounding medium and leading to a reduction in shear modulus not only locally but also triggered by the propagating waves. This damage-induced softening releases further energy that redistributes the stress ahead of the damaged region and triggers further ruptures and damage propagation. As a result, we observe that the damage forms band-like structures at these fault junctions, propagating further and connecting with other damage bands, eventually forming a complementary network to the pre-existing fault network. This suggests that, under some conditions, a pre-existing fault network may not be enough to accommodate the deformation and the emergence of new fault segments become necessary.

Finally, it is interesting to note the complex wave fields that is radiated from the tips of the damage bands, as shown in Fig.7(c). The propagation of damage bands into the surrounding intact media degrades the material and triggers the transition into a granular phase. Since this material degradation occurs on inertial time scales, it radiates waves akin to dynamic Eshelby inclusions (Ni and Markenscoff, 2016) and analytical results on seismic radiation from regions sustaining rapid changes of elastic moduli (Ben-Zion and Ampuero, 2009; Ben-Zion and Lyakhovsky, 2019). The damage related radiation interferes with the waves resulting from the slip on the fault network and leads to constructive interference patterns and wave reverberations that enhance high frequency radiation. This particular feature is prominent behind the rupture front, where the reduction of elastic modlui is significant and can affect the subsequent rupture physics as discussed in the next section. The damage related radiation distinguishes our CDB model from plasticity models where the elastic moduli remain unchanged.

4. Discussion and Conclusions

We integrate the continuum damage-breakage (CDB) model with the linear slip weakening friction law within the MOOSE-FARMS software for the 2D in-plane case. The numerical framework is used to conduct initial simulations of interactions of dynamic ruptures with off-fault damage and bulk instabilities, particularly focusing on the transition during brittle instabilities to granular flow within various pre-existing fault zone geometries. The results show that damage accumulates predominantly within regions of stress concentrations, as expected, with preference to zones experiencing tensile stress perturbations. Upon reaching a critical damage threshold, a phase transition into granular flow occurs. This process results in the localized formation and propagation of a granular phase, the extent of which is governed by specific rate coefficients (C_d, C_B). Additionally, we observe that certain fault geometries, such as dead-end corners and fault intersections, can expedite damage-breakage development. When a rupture is halted in these areas, it creates strong stress concentrations and discharges considerable energy, thus intensifying damage generation and granular localization in addition to seismic waves reverberations. This is consistent with results associated with off-fault yielding in the form of plasticity (Xu and Ben-Zion, 2013; Abdelmeguid and Elbanna, 2022a). However, our simulations with the CDB rheology accounting for reduction of elastic moduli in yielding regions produce additional important features discussed further below.

Our investigation includes detailed comparisons of results with the widely-used Drucker-Prager plasticity model for simulating off-fault plasticity. The reduced shear modulus in the CDB model, not accounted for by plasticity models, produces zones with altered wave velocities around the fault consistent with field observations (Ben-Zion and Sammis, 2003). Upon reaching a specific damage threshold, the damaged material becomes unstable and transitions into a granular phase. The continuum damage-breakage model successfully captures the formation of conjugate bands, whereas the Drucker-Prager model only yields for comparable strength parameters distributed inelastic deformation. Moreover, the dynamic reduction of the shear modulus alters and reflects the radiated wave field behind the rupture tip, influencing slip and slip rate profiles and enhancing seismic radiation. The damage related radiation changes dynamically the normal stress on the fault, and thus may have strong effects on the energy partitioning during failure and various features generated by the rupture. Field observations at close proximity to earthquakes show relatively high ratios of P-wave/S-wave energy and isotropic source components consistent with expectations for damage related radiation (Kwiatek and Ben-Zion, 2013; Cheng et al., 2021).

The adopted CDB model includes a healing mechanism following the reduction of stress upon failure, which is demonstrated to be capable of cessation or reversal of cohesive granular flow under some circumstances. This healing mechanism complements other healing mechanisms that may exist in the subsurface during the long interseismic period such as those facilitated by chemical reactions or temperature effects. Capturing elasticity and strength recovery, as enabled by the CDB model, is important for consistent modeling of fault zone evolution over seismic cycles where healing occur on multiple time scales including during rapid stress unloading and during the slow interseismic deformation period.

The stress perturbations induced by activated ruptures play a critical role in promoting the triggering of failure at other potential faults within these networks. We observe that the patterns of damage-breakage are notably localized. These patterns emerge predominantly from intersections and are expected to expand off-fault, potentially connecting with other bands to form an intricate evolving network. This phenomenon is noteworthy, particularly in how the localized damage-breakage aligns with the overall fault network dynamics and explore new paths not traced by the pre-existing fault surfaces. Despite the pronounced impact of local stress field perturbations, we observe preferred directions for the extension of these bands. These directions make an acute angle relative to the maximum principal stress direction, in line with our earlier discussion on the conjugate faulting associated with the planar fault case, offering insights into the underlying mechanics of fault network evolution and interaction. Our results provide new insights that complement other valuable work on rupture dynamics of fault networks (e.g. (Palgunadi et al., 2024)), which suggests the critical role of size-dependent fracture energy in facilitating rupture cascades. Here, we further emphasize the role of off-fault damage and dynamic growth of fault segments in providing additional mechanisms for stress redistribution and energy transfer beyond the capacity of on-fault friction evolution.

In this study we considered initially homogeneous elastic properties to primarily focus on salient effects of off-fault damage-breakage on rupture characteristics. However, material heterogeneity is often observed in the field. Such heterogeneity may interact with the damage evolution at different levels. For example, elastic heterogeneities influence wave propagation causing reflections and diffraction which may lead to spatially heterogeneous focusing and scattering effects that may influence damage and healing. Damage band propagation in layered media is expected to be more complex as interfaces with different strength properties may deflect or arrest incoming bands. Bimaterial interfaces can affect the mode and propagation of earthquake ruptures (Andrews and Ben-Zion, 1997; Ben-Zion, 2001; Ampuero and Ben-Zion, 2008; Shlomai and Fineberg, 2016), can attract ruptures that start at other locations (Brietzke and Ben-Zion, 2006) and affect long-term earthquake cycles (Abdelmeguid and Elbanna, 2022a). Consideration of more realistic velocity structures will be investigated in future studies using data from the community velocity models of the Statewide California Earthquake Center (SCEC).

In this study we have used the linear slip weakening law as a model for fault friction. Alternative frictional formulations include the rate-and-state friction law that has been successful in capturing rate sensitivity, spontaneous nucleation, aseismic slip, and post-seismic relaxation. Unlike the linear slip-weakening law, where the friction coefficient μ decreases linearly with slip, the friction coefficient in the rate-and-state friction law depends on both the slip rate V and a set of state variables θ that encapsulate the history of slip rate evolution. The introduction of slip rate dependence captures both friction strengthening and weakening, while the state variable allows for the repetition of steady sliding and transient slip processes. This makes the rate-and-state friction law suitable for simulating earthquake cycles. For single dynamic rupture simulations, which are the focus of this paper, choosing appropriate rate-weakening parameters $(a, b; a < b)$ in rate-and-state friction can produce a similar stress-slip curve to linear slip weakening response with comparable magnitude, see (Luo and Duan, 2018) for detailed comparison of various friction laws. However, the rate dependence of friction may be critical in some applications. For example, enhanced dynamic weakening at co-seismic slip rates due to shear heating effects, including flash heating and thermal pressurization, was shown to affect the rupture mode (i.e. pulses vs cracks), peak slip rates, rupture speed, temperature rise on the fault surface, and amplitude of dynamic stress drop. These in turn may affect the intensity and extent of co-seismic damage generation and thermally-activated flow. In this study, we have focused on varying the effect of fault zone architecture and damage model parameters in controlling the co-seismic evolution of off-fault material properties for a given fault friction model. Future work will consider additional frictional effects including rate dependence and shear heating.

We limited our investigation to problems in the 2D plane strain configuration. A 3D computational model that includes CDB rheology in the bulk will provide a more realistic framework for studying a range of fundamental topics in the physics of earthquakes and faults, including the organization of fracture network, stress, and strain in the periods leading to large failure events. Most importantly, extension to 3D will enable consideration of depth dependent overburden pressure, pore pressure, and temperature profiles. At depth, higher pressures may decrease the potential for damage generation. However, the reduction of elastic moduli in damage zones produces isotropic radiation with amplitude that increases with the initial elastic strain (and hence depth) that can produce further rock damage and fragmentation (Ben-Zion and Ampuero, 2009; Ben-Zion and Lyakhovsky, 2019). Also, if the dyanmic stress drop increases with depth that could promote damage. Elevated temperatures and pore pressures at depth may promote healing. However, higher temperatures may also allow increased inelastic deformation enabled by thermally activated processes. Investigation of these competing mechanisms will provide novel insights into earthquake source physics. Such modeling could suggest refined observables that may be used to track processes associated with degradation and recovery of elastic moduli within fault zones, and elucidating the mechanisms underlying fault zone maturation and different space-time seismicity patterns. This research trajectory is anticipated to offer significant insights into the behavior of fault systems over different time scales, with important implications for next generation seismic hazard models.

The results presented in this study constitute an initial investigation into the effects of bulk damage-breakage on the dynamics of rupture propagation within complex fault zones. The discussed problems represent a potentially interesting area for collaboration between researchers from mechanics, material science, and earthquake sciences. The results point to a realm of unresolved research questions that warrant further exploration. Critical among these is the need for an in-depth analysis of the influence of the damage-breakage phenomena on energy partitioning, particularly examining the competition between energy dissipation via inelastic deformation and damage generation on one hand, and enhanced seismic radiation due to dynamic reduction of normal stress in the rupture zone along with the additional radiation ensuing from excess strain energy in regions sustaining dynamic reduction of elastic moduli. An advanced investigation into characteristics of the radiated wave field, including its tensorial composition and frequency spectrum, is needed for a more nuanced understanding of the interaction between the seismic wavefield and rupture properties. Important goals of the continuing research are generalizing the simulation framework to three dimensions and to long histories accounting for evolutionary processes. This presents significant, but not insurmountable computational challenges.

5. Acknowledgments

It is a privilege to contribute this paper to the special volume in honor of Alan Needleman whose pioneering works in mechanics and numerical modeling paved the way to many works including some of ours. The paper benefited from insightful comments by Shiqing Xu, two anonymous referees and the editor Ghatu Subhash. The study was supported by the National Science Foundation (grants EAR-1753249, OAC-2311207, and OAC-2311206) and the Southern/Statewide California Earthquake Center (based on NSF Cooperative Agreement EAR-1600087 and USGS Cooperative Agreement G17AC00047). We are grateful to the Idaho National Lab for providing High performance computing support and access and for the MOOSE/Falcon team for offering technical support. We also acknowledge funding provided by DOE EERE Geothermal Technologies Office to Utah FORGE and the University of Utah under Project DE-EE0007080 Enhanced Geothermal System Concept Testing and Development at the Milford City, Utah Frontier Observatory for Research in Geothermal Energy (Utah FORGE) site.

6. References

References

Abdelmeguid, M., Elbanna, A., 2022a. Modeling sequences of earthquakes and aseismic slip (seas) in elasto-plastic fault zones with a hybrid finite element spectral boundary integral scheme. Journal of Geophysical Research: Solid Earth 127, e2022JB024548.

Abdelmeguid, M., Elbanna, A., 2022b. Sequences of seismic and aseismic slip on bimaterial faults show dominant rupture asymmetry and potential for elevated seismic hazard. Earth and Planetary Science Letters 593, 117648.

Abdelmeguid, M., Zhao, C., Yalcinkaya, E., Gazetas, G., Elbanna, A., Rosakis, A., 2023. Dynamics of episodic supershear in the 2023 m7. 8 kahramanmaraş/pazarcik earthquake, revealed by near-field records and computational modeling. Communications Earth & Environment 4, 456.

Aben, F.M., Brantut, N., Mitchell, T.M., David, E.C., 2019. Rupture energetics in crustal rock from laboratory-scale seismic tomography. Geophysical Research Letters 46, 7337–7344.

Aichele, J., Latour, S., Catheline, S., Roux, P., 2023. Dynamic full-field imaging of rupture radiation: Material contrast governs source mechanism. Geophysical Research Letters 50, e2022GL100473.

Allam, A., Ben-Zion, Y., Kurzon, I., Vernon, F., 2014. Seismic velocity structure in the hot springs and trifurcation areas of the san jacinto fault zone, california, from double-difference tomography. Geophysical Journal International 198, 978–999.

Ampuero, J.P., Ben-Zion, Y., 2008. Cracks, pulses and macroscopic asymmetry of dynamic rupture on a bimaterial interface with velocity-weakening friction. Geophysical Journal International 173, 674–692.

Andrews, D., 1976. Rupture velocity of plane strain shear cracks. Journal of Geophysical Research 81, 5679–5687.

Andrews, D., 2005. Rupture dynamics with energy loss outside the slip zone. Journal of Geophysical Research: Solid Earth 110.

Andrews, D.J., Ben-Zion, Y., 1997. Wrinkle-like slip pulse on a fault between different materials. Journal of Geophysical Research: Solid Earth 102, 553–571.

Bao, H., Ampuero, J.P., Meng, L., Fielding, E.J., Liang, C., Milliner, C.W., Feng, T., Huang, H., 2019. Early and persistent supershear rupture of the 2018 magnitude 7.5 palu earthquake. Nature Geoscience 12, 200–205.

Bao, H., Xu, L., Meng, L., Ampuero, J.P., Gao, L., Zhang, H., 2022. Global frequency of oceanic and continental supershear earthquakes. Nature Geoscience 15, 942–949.

Bazant, Z.P., Jirásek, M., 2002. Nonlocal integral formulations of plasticity and damage: survey of progress. Journal of engineering mechanics 128, 1119–1149.

Ben-Zion, Y., 2001. Dynamic ruptures in recent models of earthquake faults. Journal of the Mechanics and Physics of Solids 49, 2209–2244.

Ben-Zion, Y., 2008. Collective behavior of earthquakes and faults: Continuum-discrete transitions, progressive evolutionary changes, and different dynamic regimes. Reviews of Geophysics 46.

Ben-Zion, Y., Aki, K., 1990. Seismic radiation from an sh line source in a laterally heterogeneous planar fault zone. Bulletin of the Seismological Society of America 80, 971–994.

Ben-Zion, Y., Ampuero, J.P., 2009. Seismic radiation from regions sustaining material damage. Geophysical Journal International 178, 1351–1356.

Ben-Zion, Y., Huang, Y., 2002. Dynamic rupture on an interface between a compliant fault zone layer and a stiffer surrounding solid. Journal of Geophysical Research: Solid Earth 107, ESE–6.

Ben-Zion, Y., Lyakhovsky, V., 2019. Representation of seismic sources sustaining changes of elastic moduli. Geophysical Journal International 217, 135–139.

Ben-Zion, Y., Sammis, C.G., 2003. Characterization of fault zones. Pure and applied geophysics 160, 677–715.

Ben-Zion, Y., Shi, Z., 2005. Dynamic rupture on a material interface with spontaneous generation of plastic strain in the bulk. Earth and Planetary Science Letters 236, 486–496.

Bhat, H.S., Biegel, R.L., Rosakis, A.J., Sammis, C.G., 2010. The effect of asymmetric damage on dynamic shear rupture propagation ii: With mismatch in bulk elasticity. Tectonophysics 493, 263–271.

Bhat, H.S., Rosakis, A.J., Sammis, C.G., 2012. A micromechanics based constitutive model for brittle failure at high strain rates .

Brietzke, G.B., Ben-Zion, Y., 2006. Examining tendencies of in-plane rupture to migrate to material interfaces. Geophysical Journal International 167, 807–819.

Cheng, Y., Wang, X., Zhan, Z., Ben-Zion, Y., 2021. Isotropic source components of events in the 2019 ridgecrest, california, earthquake sequence. Geophysical Research Letters 48, e2021GL094515.

Cochard, A., Rice, J., 2000. Fault rupture between dissimilar materials: Ill-posedness, regularization, and slip-pulse response. Journal of Geophysical Research: Solid Earth 105, 25891–25907.

Dansereau, V., Shapiro, N.M., Campillo, M., Weiss, J., 2023. Modeling multi-scale deformation cycles in subduction zones with a continuum visco-elastic-brittle framework. Authorea Preprints .

Das, S., Aki, K., 1977. A numerical study of two-dimensional spontaneous rupture propagation. Geophysical journal international 50, 643–668.

Day, S.M., Dalguer, L.A., Lapusta, N., Liu, Y., 2005. Comparison of finite difference and boundary integral solutions to three-dimensional spontaneous rupture. Journal of Geophysical Research: Solid Earth 110.

Duan, B., Day, S.M., 2008. Inelastic strain distribution and seismic radiation from rupture of a fault kink. Journal of Geophysical Research: Solid Earth 113.

Dunham, E.M., 2007. Conditions governing the occurrence of supershear ruptures under slip-weakening friction. Journal of Geophysical Research: Solid Earth 112.

Dunham, E.M., Archuleta, R.J., 2004. Evidence for a supershear transient during the 2002 denali fault earthquake. Bulletin of the Seismological Society of America 94, S256–S268.

Dunham, E.M., Belanger, D., Cong, L., Kozdon, J.E., 2011. Earthquake ruptures with strongly rate-weakening friction and off-fault plasticity, part 1: Planar faults. Bulletin of the Seismological Society of America 101, 2296–2307.

Einav, I., 2007a. Breakage mechanics—part i: theory. Journal of the Mechanics and Physics of Solids 55, 1274–1297.

Einav, I., 2007b. Breakage mechanics—part ii: Modelling granular materials. Journal of the Mechanics and Physics of Solids 55, 1298–1320.

Erickson, B.A., Dunham, E.M., Khosravifar, A., 2017. A finite difference method for off-fault plasticity throughout the earthquake cycle. Journal of the Mechanics and Physics of Solids 109, 50–77.

Fei, F., Mia, M.S., Elbanna, A.E., Choo, J., 2023. A phase-field model for quasi-dynamic nucleation, growth, and propagation of rate-and-state faults. International Journal for Numerical and Analytical Methods in Geomechanics 47, 187–211.

Froment, B., Campillo, M., Chen, J., Liu, Q., 2013. Deformation at depth associated with the 12 may 2008 mw 7.9 wenchuan earthquake from seismic ambient noise monitoring. Geophysical Research Letters 40, 78–82.

Gabriel, A.A., Ampuero, J.P., Dalguer, L., Mai, P.M., 2013. Source properties of dynamic rupture pulses with off-fault plasticity. Journal of Geophysical Research: Solid Earth 118, 4117–4126.

Gupta, I.N., 1973. Seismic velocities in rock subjected to axial loading up to shear fracture. Journal of Geophysical Research 78, 6936–6942.

Hamiel, Y., Liu, Y., Lyakhovsky, V., Ben-Zion, Y., Lockner, D., 2004. A viscoelastic damage model with applications to stable and unstable fracturing. Geophysical Journal International 159, 1155–1165.

Harris, R.A., Barall, M., Archuleta, R., Dunham, E., Aagaard, B., Ampuero, J.P., Bhat, H., Cruz-Atienza, V., Dalguer, L., Dawson, P., et al., 2009. The scec/usgs dynamic earthquake rupture code verification exercise. Seismological Research Letters 80, 119–126.

Hayek, J.N., May, D.A., Pranger, C., Gabriel, A.A., 2023. A diffuse interface method for earthquake rupture dynamics based on a phase-field model .

Hetland, E., Hager, B., 2005. Postseismic and interseismic displacements near a strike-slip fault: A two-dimensional theory for general linear viscoelastic rheologies. Journal of Geophysical Research: Solid Earth 110.

Huang, Y., Ampuero, J.P., 2011. Pulse-like ruptures induced by low-velocity fault zones. Journal of Geophysical Research: Solid Earth 116.

Ida, Y., 1972. Cohesive force across the tip of a longitudinal-shear crack and griffith's specific surface energy. Journal of Geophysical Research 77, 3796–3805.

Kaneko, Y., Fialko, Y., 2011. Shallow slip deficit due to large strike-slip earthquakes in dynamic rupture simulations with elasto-plastic off-fault response. Geophysical Journal International 186, 1389–1403.

Kurzon, I., Lyakhovsky, V., Ben-Zion, Y., 2019. Dynamic rupture and seismic radiation in a damage–breakage rheology model. Pure and Applied Geophysics 176, 1003–1020.

Kurzon, I., Lyakhovsky, V., Ben-Zion, Y., 2021. Earthquake source properties from analysis of dynamic ruptures and far-field seismic waves in a damage-breakage model. Geophysical Journal International 224, 1793–1810.

Kwiatek, G., Ben-Zion, Y., 2013. Assessment of p and s wave energy radiated from very small shear-tensile seismic events in a deep south african mine. Journal of Geophysical Research: Solid Earth 118, 3630–3641.

Lindsay, A.D., Gaston, D.R., Permann, C.J., Miller, J.M., Andrš, D., Slaughter, A.E., Kong, F., Hansel, J., Carlsen, R.W., Icenhour, C., et al., 2022. 2.0-moose: Enabling massively parallel multiphysics simulation. SoftwareX 20, 101202.

Lockner, D., Byerlee, J., 1980. Development of fracture planes during creep in granite .

Luo, B., Duan, B., 2018. Dynamics of nonplanar thrust faults governed by various friction laws. Journal of Geophysical Research: Solid Earth 123, 5147–5168.

Lyakhovsky, V., Ben-Zion, Y., 2014a. A continuum damage–breakage faulting model and solid-granular transitions. Pure and Applied Geophysics 171, 3099–3123.

Lyakhovsky, V., Ben-Zion, Y., 2014b. Damage–breakage rheology model and solid-granular transition near brittle instability. Journal of the Mechanics and Physics of Solids 64, 184–197.

Lyakhovsky, V., Ben-Zion, Y., Agnon, A., 1997. Distributed damage, faulting, and friction. Journal of Geophysical Research: Solid Earth 102, 27635–27649.

Lyakhovsky, V., Ben-Zion, Y., Agnon, A., 2005. A viscoelastic damage rheology and rate-and state-dependent friction. Geophysical Journal International 161, 179–190.

Lyakhovsky, V., Ben-Zion, Y., Ilchev, A., Mendecki, A., 2016. Dynamic rupture in a damage-breakage rheology model. Geophysical Journal International 206, 1126–1143.

Lyakhovsky, V., Hamiel, Y., Ben-Zion, Y., 2011. A non-local visco-elastic damage model and dynamic fracturing. Journal of the Mechanics and Physics of Solids 59, 1752–1776.

Lysmer, J., Kuhlemeyer, R.L., 1969. Finite dynamic model for infinite media. Journal of the engineering mechanics division 95, 859–877.

Ma, S., Andrews, D., 2010. Inelastic off-fault response and three-dimensional dynamics of earthquake rupture on a strike-slip fault. Journal of Geophysical Research: Solid Earth 115.

Mia, M.S., Abdelmeguid, M., Elbanna, A.E., 2022. Spatio-temporal clustering of seismicity enabled by off-fault plasticity. Geophysical Research Letters 49, e2021GL097601.

Mia, M.S., Abdelmeguid, M., Elbanna, A.E., 2023. The spectrum of fault slip in elastoplastic fault zones. Earth and Planetary Science Letters 619, 118310.

Needleman, A., 1988. Material rate dependence and mesh sensitivity in localization problems. Computer methods in applied mechanics and engineering 67, 69–85.

Nguyen, V.P., 2014. An open source program to generate zero-thickness cohesive interface elements. Advances in Engineering Software 74, 27–39.

Ni, L., Markenscoff, X., 2016. The dynamic generalization of the eshelby inclusion problem and its static limit. Proceedings of the Royal Society A: Mathematical, Physical and Engineering Sciences 472, 20160256.

Okubo, K., Bhat, H.S., Rougier, E., Marty, S., Schubnel, A., Lei, Z., Knight, E.E., Klinger, Y., 2019. Dynamics, radiation, and overall energy budget of earthquake rupture with coseismic off-fault damage. Journal of Geophysical Research: Solid Earth 124, 11771–11801.

Palgunadi, K.H., Gabriel, A.A., Garagash, D.I., Ulrich, T., Mai, P.M., 2024. Rupture dynamics of cascading earthquakes in a multiscale fracture network. Journal of Geophysical Research: Solid Earth 129, e2023JB027578.

Palmer, A.C., Rice, J.R., 1973. The growth of slip surfaces in the progressive failure of over-consolidated clay. Proceedings of the Royal Society of London. A. Mathematical and Physical Sciences 332, 527–548.

Pei, S., Niu, F., Ben-Zion, Y., Sun, Q., Liu, Y., Xue, X., Su, J., Shao, Z., 2019. Seismic velocity reduction and accelerated recovery due to earthquakes on the longmenshan fault. Nature Geoscience 12, 387–392.

Peng, Z., Ben-Zion, Y., 2006. Temporal changes of shallow seismic velocity around the karadere-düzce branch of the north anatolian fault and strong ground motion. Pure and Applied Geophysics 163, 567–600.

Poliakov, A.N., Dmowska, R., Rice, J.R., 2002. Dynamic shear rupture interactions with fault bends and off-axis secondary faulting. Journal of Geophysical Research: Solid Earth 107, ESE–6.

Qiu, H., Ben-Zion, Y., Catchings, R., Goldman, M.R., Allam, A.A., Steidl, J., 2021. Seismic imaging of the mw 7.1 ridgecrest earthquake rupture zone from data recorded by dense linear arrays. Journal of Geophysical Research: Solid Earth 126, e2021JB022043.

Ren, C., Wang, Z., Taymaz, T., Hu, N., Luo, H., Zhao, Z., Yue, H., Song, X., Shen, Z., Xu, H., et al., 2024. Supershear triggering and cascading fault ruptures of the 2023 kahramanmaraş, türkiye, earthquake doublet. Science 383, 305–311.

Rice, J.R., Sammis, C.G., Parsons, R., 2005. Off-fault secondary failure induced by a dynamic slip pulse. Bulletin of the Seismological Society of America 95, 109–134.

Rousseau, C.E., Rosakis, A.J., 2009. Dynamic path selection along branched faults: Experiments involving sub-rayleigh and supershear ruptures. Journal of Geophysical Research: Solid Earth 114.

Rudnicki, J.W., Rice, J., 1975. Conditions for the localization of deformation in pressure-sensitive dilatant materials. Journal of the Mechanics and Physics of Solids 23, 371–394.

Shi, Z., Needleman, A., Ben-Zion, Y., 2010. Slip modes and partitioning of energy during dynamic frictional sliding between identical elastic–viscoplastic solids. International Journal of Fracture 162, 51–67.

Shlomai, H., Fineberg, J., 2016. The structure of slip-pulses and supershear ruptures driving slip in bimaterial friction. Nature communications 7, 11787.

Spudich, P., Olsen, K., 2001. Fault zone amplified waves as a possible seismic hazard along the calaveras fault in central california. Geophysical Research Letters 28, 2533–2536.

Stanchits, S., Vinciguerra, S., Dresen, G., 2006. Ultrasonic velocities, acoustic emission characteristics and crack damage of basalt and granite. Pure and Applied Geophysics 163, 975–994.

Sun, T., Wang, K., 2015. Viscoelastic relaxation following subduction earthquakes and its effects on afterslip determination. Journal of Geophysical Research: Solid Earth 120, 1329–1344.

Templeton, E.L., Rice, J.R., 2008. Off-fault plasticity and earthquake rupture dynamics: 1. dry materials or neglect of fluid pressure changes. Journal of Geophysical Research: Solid Earth 113.

Thakur, P., Huang, Y., 2021. Influence of fault zone maturity on fully dynamic earthquake cycles. Geophysical Research Letters 48, e2021GL094679.

Thomas, M.Y., Bhat, H.S., 2018. Dynamic evolution of off-fault medium during an earthquake: a micromechanics based model. Geophysical Journal International 214, 1267–1280.

Veeraraghavan, S., Bolisetti, C., Slaughter, A., Coleman, J., Dhulipala, S., Hoffman, W., Kim, K., Kurt, E., Spears, R., Munday, L., 2021. Mastodon: an open-source software for seismic analysis and risk assessment of critical infrastructure. Nuclear Technology 207, 1073–1095.

Wang, K., Hu, Y., He, J., 2012. Deformation cycles of subduction earthquakes in a viscoelastic earth. Nature 484, 327–332.

Weertman, J., 1980. Unstable slippage across a fault that separates elastic media of different elastic constants. Journal of Geophysical Research: Solid Earth 85, 1455–1461.

Xu, S., Ben-Zion, Y., 2013. Numerical and theoretical analyses of in-plane dynamic rupture on a frictional interface and off-fault yielding patterns at different scales. Geophysical Journal International 193, 304–320.

Xu, S., Ben-Zion, Y., Ampuero, J.P., Lyakhovsky, V., 2015. Dynamic ruptures on a frictional interface with off-fault brittle damage: feedback mechanisms and effects on slip and near-fault motion. Pure and Applied Geophysics 172, 1243–1267.

Xu, S., Fukuyama, E., Yamashita, F., Takizawa, S., 2019. Evolution of fault-interface rayleigh wave speed over simulated earthquake cycles in the lab: Observations, interpretations, and implications. Earth and Planetary Science Letters 524, 115720.

Xu, X.P., Needleman, A., 1994. Numerical simulations of fast crack growth in brittle solids. Journal of the Mechanics and Physics of Solids 42, 1397–1434.

Zigone, D., Ben-Zion, Y., Campillo, M., Roux, P., 2015. Seismic tomography of the southern california plate boundary region from noise-based rayleigh and love waves. Pure and Applied Geophysics 172, 1007–1032.

Appendix A. Appendix

Appendix A.1. Spring-dashpot block representation

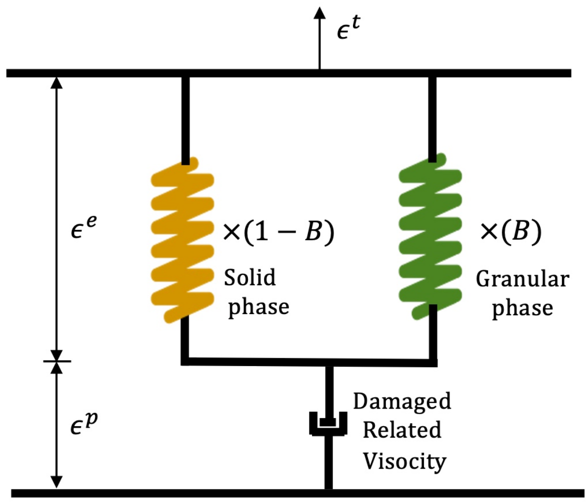

Figure A.1: **Spring-dashpot block representation of continuum damage-breakage model. As depicted in the figure, the spring-dashpot system is two parallel springs connects in series of a dashpot. The contribution from the two springs, either solid phase (yellow spring) or granular phase (green spring), is governed by the elastic strain ϵ^e, and is partitioned by breakage parameter B. The dashpot represents damage-related viscosity, produces permanent strain ϵ^p. Thus the total strain is partitioned into elastic strain (parallel springs) and permanent strain (dashpot).**

Appendix A.2. Continuum damage-breakage model derivation

The strain invariant ratio at onset of damage evolution ξ_o is a material property related to the internal friction angle ϕ (Xu et al., 2015):

$$\xi_o = \frac{-\sqrt{2}}{\sqrt{1 + (\lambda/\mu_o + 1)^2 sin^2\phi}} \tag{A.1}$$

The transition from solid to granular phase takes place at a certain critical damage variable value α_{cr}. This boundary is determined by the loss of convexity in the solid phase, see (Lyakhovsky and Ben-Zion, 2014b), section 3.2. A critical strain invariant ratio ξ_1 is determined by the convexity loss condition, the equation is shown below:

$$\xi_1 = \xi_o + \sqrt{\xi_o^2 + 2\frac{\mu_o}{\lambda_o}} \tag{A.2}$$

The probability function $P(\alpha)$ has the form:

$$P(\alpha) = \frac{1}{exp(\frac{\alpha_{cr}(\xi)-\alpha}{\beta}) + 1} \tag{A.3}$$

The presence of $P(\alpha)$ in the breakage parameter evolution equation is to control the timing for transition to take place. The transition takes place when the damage variable α approaches α_{cr}, this is considered in the exponent term in equation (A.3) such that $P(\alpha << \alpha_{cr}) \rightarrow 0$ and $P(\alpha > \alpha_{cr}) \rightarrow 1$. β is the width of transition region, if $\beta \rightarrow 0$, $P(\alpha)$ approaches Heaviside function, otherwise a finite transition region (or mushy region combines both phases where $0 < B < 1$) is presented to smooth the rapid change from solid phase to granular phase.

Appendix A.3. Planar fault particle velocity time snapshots

We compare the particle velocity time snapshots in two models with identical geometry and boundary conditions but one is governed by linear elastic material response while the other is governed by the CDB model. The rupture in both cases is right-lateral. For the linear elastic material, the constitutive equation takes the following form:

$$\sigma_{ij} = \lambda I_1 \delta_{ij} + 2\mu\epsilon_{ij} \tag{A.4}$$

Here the elastic moduli remain constant. From Fig.A.2(a), we observe that the linear elastic case exhibits clear bi-lateral supershear propagation Mach cones on both sides of the fault. However, as shown in Fig.A.2(b), on the tensile side in the CDB model, the velocity profile is more diffuse with lower magnitude of the velocities carried by the Mach cone compared with linear elastic case due to the interaction with the co-seismically generated damage. The emergence of granular bands at the rupture tip also distorts the Mach cone.

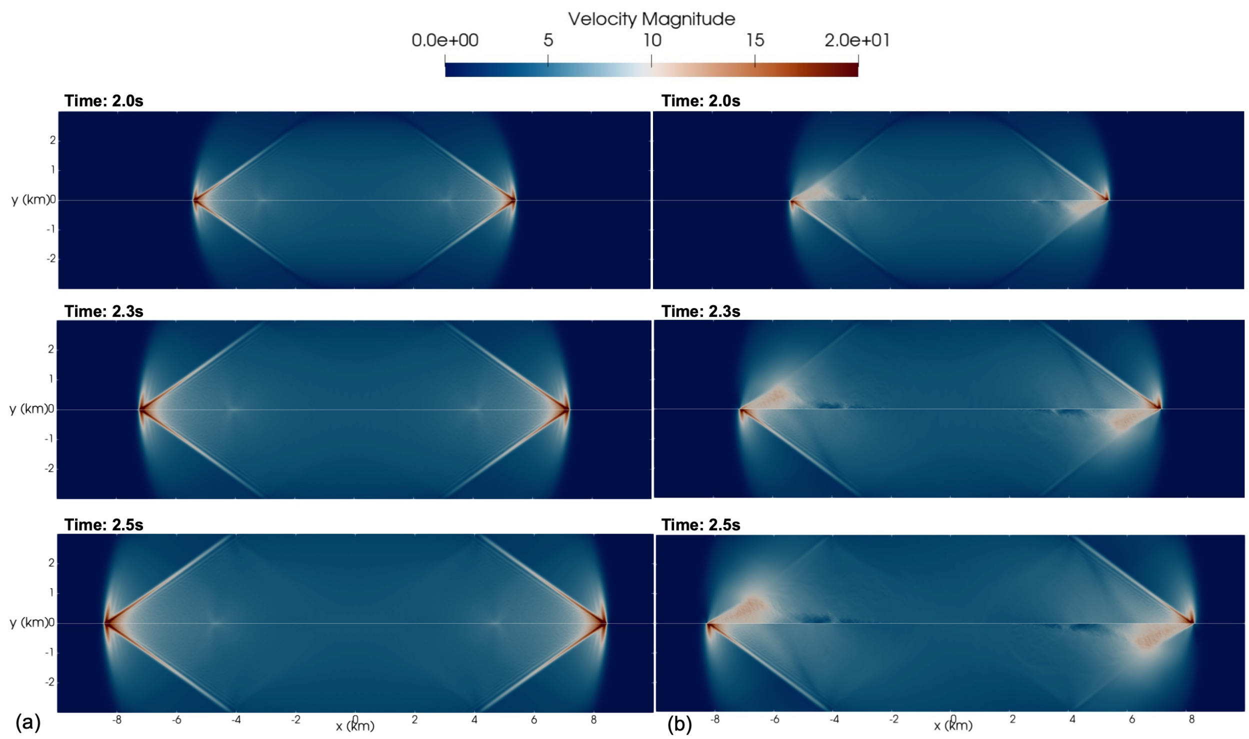

Figure A.2: **Particle Velocity Time Snapshots. (a) Linear elastic case. (b) Continuum damage-breakage model.**

Appendix A.4. Dynamic rotation of the principal stresses

As shown in Fig.A.3(a), the initial maximum principal stress is uniform across the domain, with its orientation points southeast direction ($\psi = -45^o$). At time equals 2.0 s, as the rupture propagates and develops as supershear, the orientation of maximum principal stress direction behind the tip rotates clockwise and become nearly vertical ($\psi \approx 90^o$) leading to the emergence of the conjugate bands, behind the rupture tip, in the directions described in the main text (See also Fig.2(b)). We also highlight the co-rotation of the minimum principal stress in Fig.A.3(b). We note that very close to the rupture tip, we also observe that the sense of the minimum compressive stress has reversed (from compressive to tensile). Please refer to main text in section 3.1 for detailed discussion.

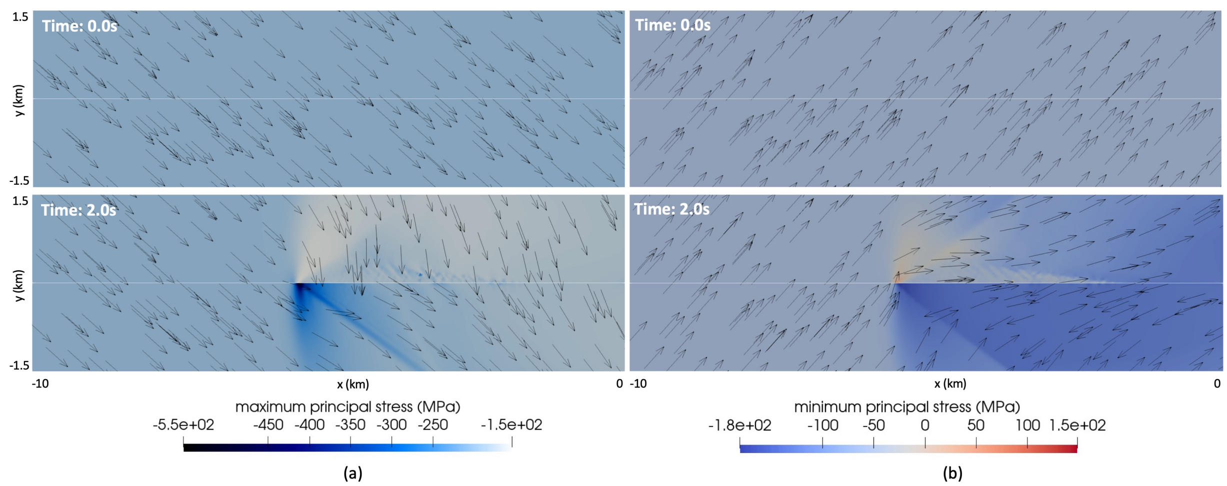

Figure A.3: **Time snapshots for the principal stress values (colormap) together with the principal stress orientation (black arrow) at t = 0.0 s and t = 2.0 s. Note: only left half of the simulation is shown, the rupture propagates from right to left. The black arrows only represent orientation, their lengths do not indicate the magnitude. (a) Maximum principal stress. (b) Minimum principal stress.**

Appendix A.5. Planar fault case with subRayleigh rupture

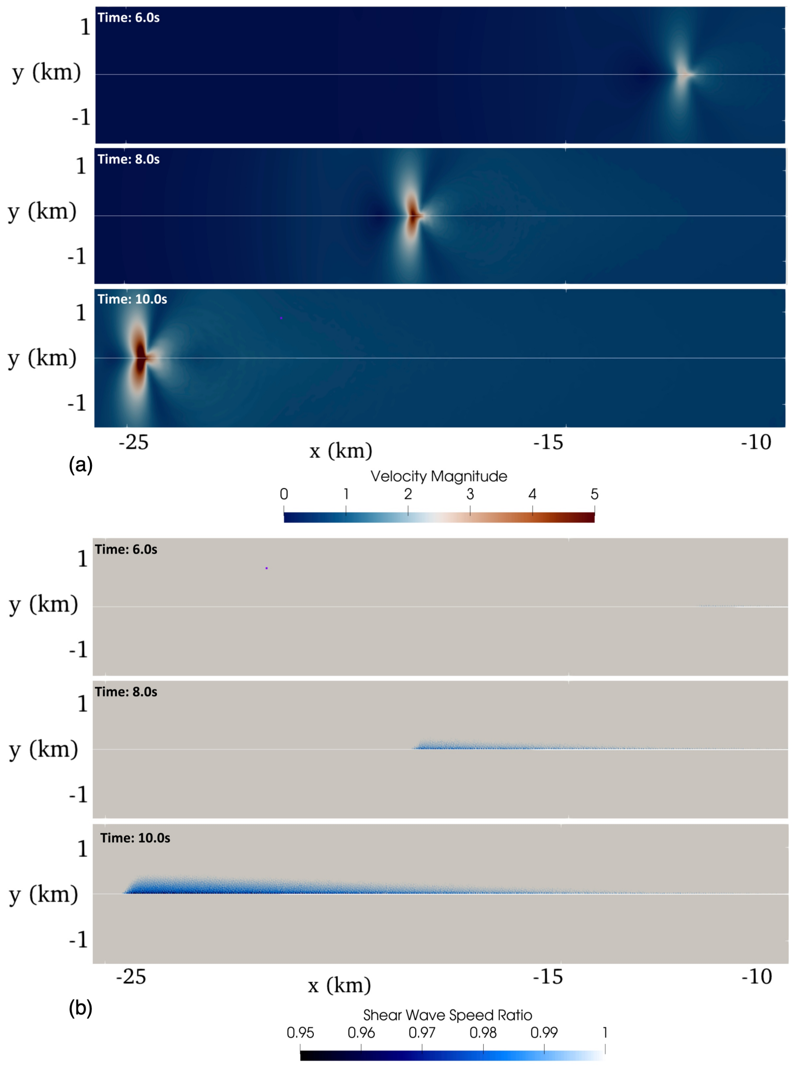

Figure A.4: **Particle velocity and shear wave speed ratio time snapshots for subRayleigh rupture case.** In this case, the strength parameter is set to be $S = 2.0$ to ensure rupture is under subRayleigh speed throughout, and we use damage rate parameter $C_d = 10^6 1/s$ in (a) where the particle velocity is shown, we observe clear and symmetry subRayleigh rupture feature without any disturbance. In (b) we show shear wave speed ratio, the damage is distributed with its maximum value is only 5 percent of the initial shear wave speed.

In this subsection, we explore the case where rupture travels with subRayleigh speed along the fault. To ensure the persistent subRayleigh feature, we perturb dynamic friction coefficient μ_d such that the strength parameter $S = (\mu_s - \mu)/(\mu - \mu_d) = 2.0$ (Dunham, 2007). The damage accumulation rate $C_d = 10^6 1/s$. Other parameters are kept the same as in section 3.1. We observe clear subRayleigh velocity profile in Fig.A.4(a) and distributed damage accumulation only without invoking any granular transition in Fig.A.4(b). The damage magnitude is much smaller than in section 3.1 where rupture propagtes in super-shear speed, with the maximum damage is only 5 percent of the shear wave speed, compared to 70 % in the supershear case with the same damage rate parameter (Fig.6(c)). This is not surprising since cases which produce super-shear features ($S = 0.2$) typically possess higher stress drop than the case shown here ($S = 2.0$) Note the findings for subRayleigh cases are quantitatively agree with previous work by (Xu et al., 2015).

Appendix A.6. Planar fault slip rate and shear stress time history plots

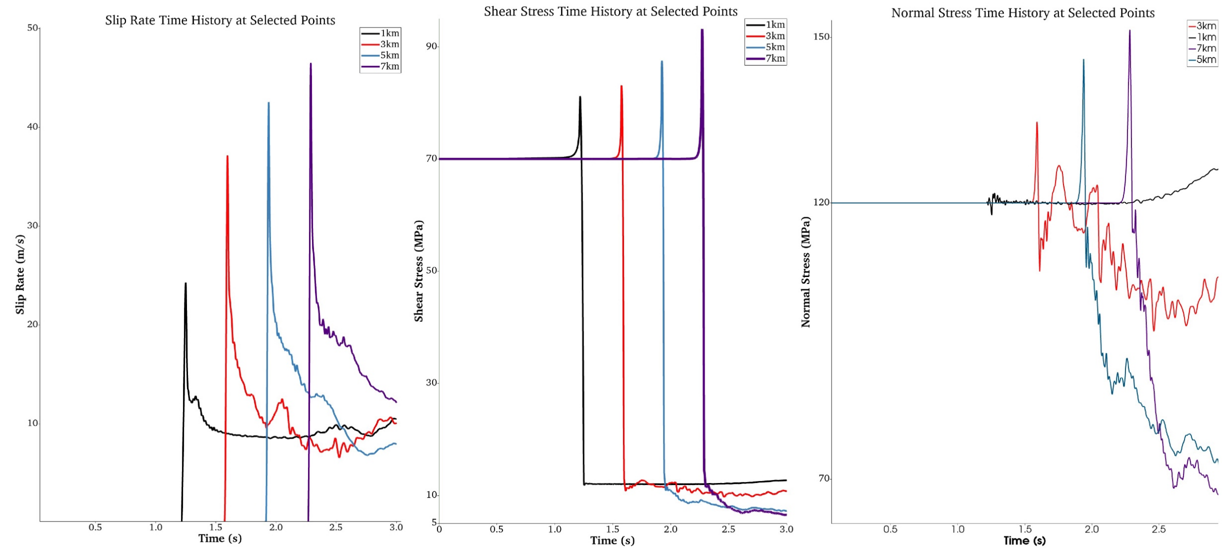

Figure A.5: **Slip rate and shear stress time history at selected points along the fault: 1km, 3km, 5km, 7km (measured with respect to the center of the fault).**

Fig. A.5 shows the slip rate, shear stress, and normal stress time histories at selected points along the fault surface at distances 1km, 3km, 5km, and 7km, respectively, away from the center of nucleation patch. From Fig.A.5(a), we observe higher peak slip rate as the rupture moves away from the nucleation region. The oscillations in slip rate profile after the peak, observed at 3km, 5km, and 7km, are the result of wave reflections from the co–seismically generated damage. From Fig.A.5(b), the increase in instantaneous peak shear stress as the rupture progresses is due to the initial increase of normal stress, as shown in Fig.A.5(c). The modulus degradation along the tensile side contributes to a bimaterial effect which promote a reduction in the normal stress behind the rupture tip and a dynamic weakening effect leading to a decrease in the residual frictional strength. At $x = 1km$, no off-damage has developed yet, the shear stress drops to residual strength, as expected for linear slip weakening friction law. After $x = 3km$, the material transits into granular phase and the decrease of normal stress further reduces the residual value of shear stress.